
Article:
Ossa Ossa, F, Hofmann, A, Wille, M et al. (5 more authors) (2018) Aerobic iron and manganese cycling in a redox-stratified Mesoarchean epicontinental sea. Earth and Planetary Science Letters, 500. pp. 28-40. ISSN 0012-821X

https://doi.org/10.1016/j.epsl.2018.07.044

Aerobic iron and manganese cycling in a redox-stratified Mesoarchean epicontinental sea

Frantz Ossa Ossa[a,b]*, Axel Hofmann[a], Martin Wille[b,c], Jorge E. Spangenberg[d], Andrey Bekker[e,a], Simon W. Poulton[f], Benjamin Eickmann[b], and Ronny Schoenberg[b]

[a]Department of Geology, University of Johannesburg, 2092 Johannesburg, South Africa

[b]Department of Geosciences, University of Tuebingen, 72074 Tuebingen, Germany

[c]Institute of Geological Sciences, University of Bern, 3012 Bern, Switzerland

[d]Institute of Earth Surface Dynamics, University of Lausanne, 1015 Lausanne, Switzerland

[e]Department of Earth Sciences, University of California, Riverside, CA 9252, USA

[f]School of Earth and Environment, University of Leeds, Leeds LS2 9JT, UK

*Correspondence to: frantz.ossaossa@gmail.com.

Abstract

Redox conditions in the marine realm prior to the Great Oxidation Event (GOE; ~2.46-2.32 Ga ago), during which the atmospheric oxygen level rose dramatically for the first time, are still debated. Here, we present C, O, Fe, and Mo stable isotope systematics of Fe-, Mn-, and carbonate-rich shales, deposited at different water depths in association with iron formations (IFs) of the Mesoarchean Mozaan Group, Pongola Supergroup, South Africa. $\delta^{13}C$ values between -22.3 and -13.5 ‰ VPDB, and $\delta^{18}O$ values between -21.1 and -8.6 ‰ VPDB for Fe-Mn-rich carbonate minerals indicate their precipitation out of equilibrium with seawater. Instead, early diagenetic reduction of Fe-Mn-oxyhydroxide precursor minerals, along with microbially induced oxidation of organic matter (OM), formed these carbonates. $\delta^{56}Fe_{IRMM-014}$ values between -1.27 and 0.14 ‰ and $\delta^{98}Mo_{NIST\ 3134+0.25}$ values between -0.46 and 0.56 ‰ co-vary with Mn concentrations and inferred water depth of deposition. This suggests that,

despite the diagenetic origin of the Fe-Mn carbonates, the primary light Fe and Mo isotopic signature of Fe-Mn-oxyhydroxides that originally precipitated from seawater is still preserved. While isotopically light Mo implies that Mn(II) was oxidized to Mn(IV) due to the availability of free, photosynthetically produced O_2, Mn enrichment suggests that the water column was redox stratified with a Mn-redoxcline situated at a depth below the storm wave base. A trend to highly negative δ^{56}Fe values with increasing Mn/Fe ratios and decreasing depositional depth suggests progressive oxidation of Fe(II) as deep-waters upwelled across a redoxcline towards shallow, well-oxygenated waters where Mn(IV) oxyhydroxides precipitated. Combined δ^{56}Fe and δ^{98}Mo data indicate pervasive oxygenation of seawater with the average O_2 content in the photic zone likely reaching levels higher than the maximum value of 10 µM usually proposed for Archean oxygen oases. Since abiotic Mn(II) oxidation is kinetically very slow in marine environments, it is likely that Mn-oxidizing microorganisms catalysed Mn-oxidation in the oxygenated Pongola surface waters during deposition of IFs. This implies that aerobic metabolism had evolved before the GOE in shallow, aquatic habitats, where it exerted a first-order control on the deposition of shallow-marine, Mn-rich iron formations.

Keywords: Mesoarchean, oxygenation, iron formations, manganese deposits, Mozaan Group, Pongola Supergroup

1. Introduction

Mass-independent fractionation of sulfur isotopes in Archean sedimentary pyrites is the most compelling evidence for an anoxic Archean atmosphere (e.g., Farquhar et al., 2000; Pavlov and Kasting, 2002; Bekker et al., 2004). However, several studies suggest that free atmospheric oxygen began to rise well before the Great Oxidation Event (GOE) (Anbar et al.,

2007; Wille et al., 2007; Lyons et al., 2014 and references therein), a time when atmospheric oxygen levels rose from $<10^{-5}$ of the present atmospheric level (PAL) to ~1−5 % of PAL between 2.46 to 2.32 Ga (e.g., Farquhar et al., 2000; Bekker et al., 2004).

Iron-rich sediments (> 15 wt.% Fe_2O_3) are widespread during the Precambrian Era, with most iron formations (IFs) deposited between 2.8 and 1.8 Ga (Bekker et al., 2014; Konhauser et al., 2017). The deposition of Fe-oxyhydroxides in IFs requires redox changes, identifying redox-sensitive elements in IFs as powerful paleoceanographic proxies for the reconstruction of past conditions of the atmosphere-hydrosphere system (e.g., Siebert et al., 2003; Rouxel et al., 2005; Beukes and Gutzmer, 2008; Konhauser et al., 2017). The main source for Fe enrichments in Archean sedimentary rocks is considered to be aqueous Fe(II) derived from submarine hydrothermal vents, which was oxidized and precipitated in the shallow parts of oceans to form IFs (e.g., Holland, 1984; Klein and Beukes, 1989; Beukes and Gutzmer, 2008). Stable isotope compositions of redox-sensitive metals (e.g., Fe and Mo) within Archean IFs have been interpreted to reflect locally oxygenated shallow-marine environments, leading to the deposition of Fe(III)–bearing minerals (Planavsky et al., 2014; Satkoski et al., 2015; Kurzweil et al., 2016). Wherever locally oxygenated surface waters were present in coastal marine environments, the water column must have been vertically stratified and laterally variable with respect to Fe concentrations (e.g., Holland, 1984; Klein and Beukes, 1989; Beukes and Gutzmer, 2008). The processes that led to the oxidation of dissolved Fe(II) to insoluble Fe(III) and precipitation of ferric oxyhydroxides in the Archean oceans remain highly debated. Two oxidation pathways are generally considered: (1) direct oxidation by anoxygenic photoferrotrophs in the photic zone (e.g., Kappler et al., 2005; Konhauser et al., 2017); and (2) Fe(II) oxidation by free, photosynthetically produced O_2 (Planavsky et al., 2014; Satkoski et al., 2015). A Fe(II) photo-oxidation pathway involving

solar UV is regarded as too insignificant to account for deposition of IFs (Konhauser et al., 2017). An ultimate biological control for deposition of the bulk of IFs is thus inferred.

Oxidation of Mn(II) to Mn(IV) requires a higher redox potential compared to Fe(II) and takes place in the presence of free O_2, with participation of an aerobic microbial catalyst (Tebo et al., 2004). Furthermore, besides O_2, Mn(IV)-oxyhydroxides are themselves strong natural oxidants that can oxidize and influence the biogeochemical cycles of other transition metals and certain non-metals, such as C and S (Tebo et al., 2004). A pre-GOE example is the IF of the ca. 2.45 Ga Koegas Subgroup (Transvaal Supergroup, South Africa) which contain appreciable Mn enrichments (Beukes and Gutzmer, 2008; Schröder et al., 2011; Kurzweil et al., 2016). Iron formation of the Koegas Subgroup is described as being deposited under an oxygenated seawater column where Mn-oxides and -oxyhydroxides have been regarded as important for aqueous Fe(II) oxidation as well as Mo shuttling (Kurzweil et al., 2016). Mn(II) oxidation by anoxygenic photosynthesizers has been proposed as an alternative process leading to Mn precipitation before the GOE (Johnson et al., 2013). Mn redox cycling and transition metal shuttling was proposed to already have operated in Mesoarchean shallow seawaters, ~500 Ma before the GOE, based on a Mo isotope study of IF of the Sinqeni Formation (Mozaan Group, Pongola Supergroup) that were deposited on a shallow, outer shelf during a period of maximum transgression (Planavsky et al., 2014).

The present study is built on this initial work (Planavsky et al., 2014), but we present additional isotope data (C, O, Fe and Mo) from shales that were deposited above and below storm wave base at the Pongola Basin scale. This allows more refined insight into the redox state of the water-column, reaching from deeper- (below the photic zone) to shallow-marine environments (photic zone), in the Pongola sea. The same applies to the mechanisms leading to the Fe and Mn enrichments in the Mozaan Group. We place particular emphasis on

identifying the role of water-column Mn mineral phases in metal cycling and biomass production.

2. Geological setting and samples

We investigated shales from two drill cores intersecting the Mozaan Group in the White Mfolozi Inlier and the Nongoma area (Fig. 1). The Pongola Supergroup is a Mesoarchaean volcano-sedimentary sequence deposited ca. 2.98–2.85 Ga on the southeastern margin of the Kaapvaal Craton, South Africa (Wilson and Zeh, 2018). It crops out in northern KwaZulu-Natal, Mpumalanga and Swaziland (Fig. 1) and is partially correlative with the Witwatersrand Supergroup (Beukes and Cairncross, 1991). The lithostratigraphic column includes two major stratigraphic units: (1) the volcano-sedimentary Nsuze Group, and (2) the predominantly siliciclastic Mozaan Group (Beukes and Cairncross, 1991; Hicks and Hofmann, 2012). Due to Phanerozoic erosion, the Mozaan Group in the White Mfolozi Inlier only consists of the Sinqeni and Ntombe formations (Fig. 1). In contrast, the stratigraphy in the Nongoma area is more complete, starting with the lowermost Sinqeni Formation to the uppermost Gabela Formation (Beukes and Cairncross, 1991; Nhleko, 2003). The Nongoma area also represents an overall more basinal and deeper depositional setting with thicker strata. Our samples are from the Sinqeni, Ntombe, and Thalu formations of these two areas (Fig. 1).

The Sinqeni Formation is characterized by predominantly shallow-marine sandstones with minor middle to outer shelf siltstones, shales and IFs (Beukes and Cairncross, 1991; Nhleko, 2003). In the White Mfolozi Inlier, drill core TSB07-26 intersects the entire 108 m thick Sinqeni Formation (Fig. 1), which consists of two sandstone units separated by a succession of ferruginous shale and IF. The lower sandstone includes (1) the laterally

discontinuous Denny Dalton Member of braided alluvial plain conglomerates and pebbly sandstones, and (2) the shallow-marine, trough cross-bedded quartz arenites of the Dipka Member (Hicks and Hofmann, 2012; Ossa Ossa et al., 2016). The upper part of this unit sits on a transgressive ravinement surface, overlain by a 6 m thick succession of lower shales, a 3 m thick IF, and upper 1 m thick shales of the Vlakhoek Member, recording sub-storm wave base deposition on a clastic sediment-starved shelf (Hicks and Hofmann, 2012; Ossa Ossa et al., 2016). The upper sandstone unit, referred to as the Kwaaiman Member, overlies shale along an erosional contact related to sea-level fall (Hicks and Hofmann, 2012; Ossa Ossa et al., 2016). The sandstones show symmetrical and interference ripple marks, mud drapes with mud cracks, and flaser lamination (Hicks and Hofmann, 2012). A decrease in the abundance of sedimentary structures, indicative of periodic exposure upwards in the stratigraphy suggests deposition in an intertidal environment gradually deepening to a shallow subtidal environment over the interval intersected in the core from the upper Sinqeni Formation to the middle Ntombe Formation (Hicks and Hofmann, 2012; Ossa Ossa et al., 2016). The upper Ntombe Formation in the drill core is characterized by interbedded dark- to medium-grey shales, with wavy and lenticular bedding, load casts, and fluid-escape structures. It is overlain by very fine-grained grey to light-grey sandstones displaying normal grading to shale and having sharp contacts with the underlying shale layers. This facies succession is consistent with tempestite or storm-induced turbidite deposition. The overall trend suggests a deepening of the depositional environment to depths just above storm wave-base. Most samples taken from the White Mfolozi Inlier were deposited above the fair-weather wave base, and consist of carbonate-bearing shales with elevated concentrations of Fe and Mn (Ossa Ossa et al., 2016). Carbonates form concretions, thin layers, and disseminations in the shale matrix are the main mineral hosts of Fe and Mn (Ossa Ossa et al., 2016).

In the Nongoma area, 450 m of the upper Sinqeni Formation were intersected by drill core PNG2 (Fig. 1). It is characterized by intercalations of fine- to coarse-grained argillaceous sandstones showing hummocky cross-stratification (HCS) and planar-laminated dark-grey shales (Nhleko, 2003). The sequence is interpreted to have been deposited in a storm-influenced subtidal to offshore setting. In this area, drill core PNG2 intersects the entire 1600 m thick Ntombe Formation, which is characterized by medium- to coarse-grained argillaceous sandstone, siltstone, and abundant dark-grey shales (Fig. 1). Sandstones mainly show HCS with minor trough cross-bedding, while shales are mainly planar-laminated. Thin IF layers of the Scotts Hill Member are developed in the upper Ntombe Formation (Fig. 1). The depositional environment may have varied from a shelf between fair- and storm-weather wave bases to a deeper offshore setting. The Thalu Formation, of which 750 m were intersected, is characterized by sedimentary facies similar to those of the underlying Ntombe Formation and includes a manganiferous IF of the Mbhoke Member (Nhleko, 2003) (Fig. 1). Our samples from drill core PNG2 consist of ferruginous shales.

3. Analytical methods

3.1. Electron probe microanalysis (EPMA)

Quantitative spot analyses of minerals were obtained on carbon-coated polished thin sections using a four spectrometer-equipped Cameca SX-100 electron probe microanalyzer. Operating conditions were 15 keV accelerating voltage, 6 nA beam current, 20 μm spot size for analyses on carbonates, and 15 keV, 20 nA, and 20 μm for oxides and silicates. Almandine (Al), diopside (Si), hematite (Fe), periclase (Mg), $SrSO_4$ (Sr), calcite (Ca),

rhodonite (Mn), orthoclase (K), $BaSO_4$ (Ba), TiO (Ti), CrO (Cr), NaCl (Na), and ZnS (Zn) were used as standards.

3.2. C and O isotope analysis

The carbonate carbon and oxygen isotope compositions ($\delta^{13}C_{carb}$ and $\delta^{18}O_{carb}$ values) were determined on aliquots of powdered whole rock samples (variable weight depending on the $CaCO_3$ content) at the Institute of Earth Surface dynamics of the University of Lausanne. Sample powders were analyzed using a Thermo Fisher Scientific Gas Bench II (Bremen, Germany) carbonate preparation device connected to a Delta Plus XL isotope ratio mass spectrometer that was operated in the continuous helium flow mode (Révész and Landwehr, 2002). The CO_2 extraction was done by reaction with anhydrous phosphoric acid at 70°C. Stable carbon isotope ratios are reported in the delta (δ) notation as the per mil (‰) deviation relative to the Vienna Pee Dee belemnite standard (VPDB). Normalization of the measured isotope ratios to the VPDB scale was performed by replicate analyses of an in-house working Carrara marble standard (UNIL-CM, $\delta^{13}C$ = 2.05 ‰; $\delta^{18}O$ = –1.70 ‰) and international reference materials (RMs) in each run. The $\delta^{13}C$ and $\delta^{18}O$ values of the reference gas and the UNIL-CM were normalized with the international standard reference materials (RMs) NBS 19 Limestone and NBS 18 Carbonatite (Brand et al., 2015). The repeatability and intermediate precision of the analyses (1 σ), monitored by replicate analyses of the laboratory standard UNIL-CM and the RMs, was better than ±0.05 ‰ for $\delta^{13}C$ and $\delta^{18}O$. The accuracy of the analyses was checked periodically through the analysis of the RMs.

Carbon isotope analysis of organic carbon ($\delta^{13}C_{org}$) and total organic carbon (TOC) contents were determined at the SIFIR laboratory (University of Manitoba) following the method described in Thomson et al. (2015). The TOC content was measured as the difference

between total carbon (TC, determined by combustion) and total inorganic carbon (TIC, determined by acidification). Powdered samples were weighed in a silver cup and, after acidification with ultra-pure 6 N HCl, were analysed for their C isotope composition on EA/IRMS. The EA/IRMS system consists of a CostechTM4010 elemental analyser coupled to a Delta V Plus isotope ratio mass spectrometer via an open-split interface (ConFlo III from Thermo Fisher Scientific, Bremen, Germany). Two international reference materials (USGS40, $\delta^{13}C$ = –26.39 ‰ and USGS41, $\delta^{13}C$ = –37.63 ‰; Brand et al., 2014) were analysed at the beginning, middle, and end of each run. To monitor the quality of sample preparation and analysis performance, the international standard USGS Green River shale SGR-1b ($\delta^{13}C_{org}$ = −29.3 ± 0.1 ‰) was treated and analysed as an unknown. Replicate analyses of the SGR-1b standard yielded a $\delta^{13}C$ value of −29.5 ± 0.1 ‰ (n = 24).

3.3. XRF analysis

Powdered samples were analysed for major elements (Fe, Al, and Mn) by X-ray fluorescence spectroscopy. Analysis was carried out on fused lithium tetraborate glass disks, using a PANalytical MagiX Pro PW2540 spectrometer. Loss on ignition (LOI) was determined after heating the samples to 950°C in a furnace for 30 min. Data are reported as elemental concentrations expressed in wt.% with a detection limit of 0.004 wt.%.

3.4. Fe and Mo isotope analysis

Fe and Mo isotope data were acquired for all shale samples from the White Mfolozi Inlier (above the storm wave base) and the Nongoma area (below the storm wave base) spanning the Sinqeni to Thalu formations. Around 1 g of powdered samples was heated to

600°C for 12 hours to ash organic compounds prior to chemical purification of Mo and Fe. Approximately 150 mg of ashed sample powders were dissolved using a mix of concentrated and distilled HF and HNO_3 at 100°C for 2 days. After evaporation at 80°C, samples were taken up in 6 M HCl and re-dissolved in closed beakers at 130°C for 2 days. Visual inspection of this solution for residual solids was performed to ensure complete sample dissolution. An aliquot containing 20 μg Fe was taken from the dissolved sample and doped with a ^{57}Fe-^{58}Fe double-spike in HCl matrix. Homogenization of sample and double-spike was ensured by heating to 100°C for 24 hours in closed beakers. Purification of Fe from the sample matrix was achieved using the anion exchange (AG1-X8, 100–200 mesh resin) method described by Schoenberg and von Blankenburg (2005). A small aliquot from the same sample digest, as for Fe isotope analysis described above, was diluted and the sample Mo concentration was determined using a ThermoFisher Scientific iCAP ICP-MS at the Isotope Geochemistry Laboratory of the University of Tuebingen. An aliquot containing 50 ng of Mo was then taken from the sample digest and doped with an appropriate amount of a ^{97}Mo-^{100}Mo double-spike. Mo was chemically purified using sequential combination of anion and cation exchange (AG-1X8, 200–400 mesh and AG-50WX8, 200–400 mesh resins) techniques, as described by Wille et al. (2013).

Purified samples were dissolved in 0.3 M HNO_3 and aspirated using a dual spray chamber system with a PFA nebulizer for Fe isotope measurements on the ThermoFisher Scientific Neptune Plus multi-collector ICP-MS at the Isotope Geochemistry Laboratory of the University of Tuebingen. Isotopic ratios were measured at high resolution, which assured the resolution of polyatomic argon interferences. Isobaric interferences on Fe isotopes were corrected by simultaneous measurement of ^{54}Cr and ^{58}Ni. Mo was measured in low-resolution mode using a CETAC Aridus II desolvating nebulizer system with a PFA self-aspirating nebulizer. The isobaric interferences on masses ^{98}Mo and ^{100}Mo were corrected by

simultaneously monitoring ^{99}Ru. An on-peak-zero baseline extraction was performed for both isotopic systems. The Fe and Mo isotopic data are reported in the δ-notation relative to IRMM-014 and NIST 3134+0.25, respectively:

$$\delta^{56}Fe = \left[\frac{\left({}^{56}Fe / {}^{54}Fe \right)_{Sample}}{\left({}^{56}Fe / {}^{54}Fe \right)_{IRMM-014}} - 1 \right] * 1000$$

$$\delta^{98}Mo = \left[\frac{\left({}^{98}Mo / {}^{95}Mo \right)_{Sample}}{\left({}^{98}Mo / {}^{95}Mo \right)_{NIST3134+0.25}} - 1 \right] * 1000$$

The long-term δ^{56}Fe reproducibility of the in-house HanFe standard is 0.287 ± 0.055 ‰ (2 SD, n = 145; Kurzweil et al., 2016). Aliquots of the HanFe standard measured during the course of this study gave an average δ^{56}Fe values of 0.289 ± 0.020 ‰ (2 SD, n = 7), which is in excellent agreement with the long-term δ^{56}Fe reproducibility and previously published values (Eickmann et al., 2018; Moeller et al., 2014; Kurzweil et al., 2016; Swanner et al., 2017; Wu et al., 2017). The average isotopic δ^{98}Mo deviation between the Johnson Matthey Company, ICP Mo standard solution, lot 602332B (Bern-Mo) and NIST 3134 of 0.249 ± 0.024 ‰ (2 SD, n = 4) during this measurement session is identical, within 2SD, to previously published values of the Tuebingen Isotope Geochemistry Laboratory (Kurzweil et al., 2015, 2016) and other research groups (e.g., Goldberg et al., 2013). NIST 3134 was set to +0.25 ‰ to allow comparison with earlier published data – which were reported against the Johnson and Matthey ICP standard 602332B (Siebert et al., 2001) – following the suggestion

of Nägler et al. (2014). Error bars for δ^{98}Mo representing the long-term reproducibility is 0.086 ‰ (Kurzweil et al., 2016).

4. Results

Fe-Mn host minerals observed in shallow-water shales are mainly represented by manganoan siderite together with ferroan rhodochrosite, kutnohorite, ankerite, and very limited occurrence of pyrite (Fig. 2). In IFs, manganoan siderite seems to be the main Fe-Mn-bearing mineral, with magnetite representing another important host of Fe (Fig. 2). In deep-water ferruginous shale, Mn concentration is very low and phyllosilicates, such as chlorite and stilpnomelane, represent the main Fe-bearing minerals, together with minor carbonate minerals. Electron microprobe analyses were performed on Mn-bearing minerals in shale and associated IF of the White Mfolozi Inlier (Fig. 2). In shale samples, Mn-bearing siderite has an average MnO concentration of 18 wt.% (and average MnO/FeO ratio of 0.5), Fe-bearing rhodochrosite shows an average MnO content of 30 wt.% (and average MnO/FeO ratio of 1.5), and kutnohorite has an average MnO concentration of 14 wt.% (and average MnO/FeO ratio of 1.4). In IF samples, Mn is mainly found in Mn-bearing siderite, which yielded an average MnO concentration of 8 wt.% (with average MnO/FeO ratio of 0.2).

The $\delta^{13}C_{carb}$ values of the shallow-water shales (above the fair-weather wave base) of the Ntombe Formation (White Mfolozi Inlier) vary between −22.3 and −13.5 ‰, whereas $\delta^{18}O_{carb}$ values range from −21.1 to −8.6 ‰ (Figs. 3 and 4; Table 1). No obvious correlation is observed between $\delta^{13}C_{carb}$ and $\delta^{18}O_{carb}$ values (Fig. 4). $\delta^{13}C_{org}$ values of the same samples vary between −37.7 and −25.4 ‰, and shift to more negative values upsection (Fig. 3; Table 1). Total inorganic carbon (TIC) contents decrease upsection from 4.1 wt.% in the lower part

to below detection limit in the upper part; total organic carbon (TOC) content is below 1 wt.% throughout the sedimentary succession (Table 1).

Shales of the White Mfolozi Inlier yielded Fe and Mn concentrations between 5 and 21 wt.% and 0 and 6 wt.%, respectively (Fig. 3; Tables 2; S1). Mo concentrations in the same samples range from 0.2 to 2 ppm. The δ^{56}Fe values for these samples are predominantly negative and vary between −1.27 and 0.14 ‰; δ^{98}Mo values vary between −0.46 and 0.41 ‰ (Figs. 3 and 5; Table 2).

In shale samples from the Nongoma area, Mn and Mo contents are lower; 0.05 to 0.31 wt.% and 0.3 to 1.8 ppm, respectively, while Fe concentrations remain high between 8.12 and 23.05 wt.% (Fig. 3; Table 2). The δ^{56}Fe values for these samples are less fractionated compared to the White Mfolozi Inlier and vary between –0.48 and 0.13 ‰ (Figs. 3 and 5; Table 2). The δ^{98}Mo values range between 0.34 and 0.56 ‰. Overall, the lightest δ^{56}Fe and δ^{98}Mo values of −1.27 ‰ and –0.46 ‰, respectively, were measured in Mn-rich, shallow-water facies of the White Mfolozi Inlier (Figs. 3, 5A-E; Table 2). Moreover, shallow-water samples with high Al_2O_3 concentrations show near-to-crustal Mo concentrations (Fig. 5F), but non-crustal δ^{56}Fe and δ^{98}Mo values (Figs. 4D and 4E) indicate that detrital/continental input did not control the Fe and Mo isotope composition of the studied sediments. Iron and molybdenum isotope values are thus authigenic signatures, closely linked to the chemistry and redox state that prevailed in the water column during deposition.

5. Discussion

5.1. Carbon and oxygen isotopes of Fe-Mn-rich carbonates as an indicator for dissimilatory microbial respiration (DMR)

The isotopic composition of carbonate minerals helps to elucidate whether the carbonates precipitated in equilibrium with seawater. Apart from anomalies in the early Paleoproterozoic and the late Neoproterozoic, $\delta^{13}C$ values of the marine dissolved inorganic carbon (DIC) pool are dominantly close to 0 ‰ for the Precambrian (e.g., Shields and Veizer, 2002). The "best preserved" Mesoarchean marine carbonates, including limestones and dolostones, were estimated to carry $\delta^{13}C$ values of +0.9 ± 2.1 ‰ VPDB, while their $\delta^{18}O$ values are around −6 ± 1 ‰ VPDB (Shields and Veizer, 2002; Eglington et al., 2003). These $\delta^{13}C$ values are broadly similar to values of 2.5 ‰ for "least altered" marine carbonates of the Pongola Supergroup, recently reported by Siahi et al. (2018). Considering that the isotope fractionation of carbon isotopes between calcite and siderite in equilibrium with the same fluid at room temperature is about −0.5 ‰ for $\delta^{13}C$, and 4 ‰ for $\delta^{18}O$ (Jiménez-López and Romanek, 2004), siderite formed in equilibrium with Archean seawater should have $\delta^{13}C$ and $\delta^{18}O$ values of +0.4 ± 2.1 ‰ and −2 ± 1 ‰ VPDB, respectively. Consequently, the highly negative $\delta^{13}C$ and $\delta^{18}O$ values of Mn-siderite in the Mozaan Group (Table 1; Figs. 3 and 4) do not record seawater composition. Instead, the negative $\delta^{13}C_{carb}$ values indicate that carbonate precipitated from a light C isotope source, such as organic matter in the sediment, while decreasing $\delta^{18}O$ values indicate that this process continued during burial diagenesis and metamorphism.

Microbial respiration (MR) of organic matter below the sediment-water interface requires electron acceptors, such as O_2, NO_3^-, SO_4^{2-}, Mn(IV)- or Fe(III)-oxyhydroxides. Although the presence of oxygen and sulfate in the shallow Pongola epicontinental sea has been inferred (Planavsky et al., 2014; Eickmann et al., 2018), their overall concentrations were likely low. High Fe and Mn concentrations associated with carbonate minerals are consistent with the scenario that Mn(IV)- and Fe(III)-oxyhydroxides formed in the photic zone and acted as electron acceptors in sediments during early diagenesis (Ossa Ossa et al.,

2016; Planavsky et al., 2014). Two pathways could thus be considered: (1) reduction of both Mn(IV)- and Fe(III)-oxyhydroxides coupled to anaerobic oxidation of organic matter, and (2) anaerobic oxidation of biogenic methane with Mn(IV)- and Fe(III)-oxyhydroxides acting as electron acceptors. The latter pathway is biologically mediated by methanotrophs and would have resulted in $\delta^{13}C_{org}$ values lower than −35 ‰, which are not observed in the bulk of the samples (see Table 1). The average $\delta^{13}C_{org}$ value for these samples is −27.7 ‰ and suggests that organic carbon was mainly derived from primary producers, such as photoautotrophs, although a trend to more negative $\delta^{13}C_{org}$ and $\delta^{13}C_{carb}$ values towards the top of the section may point to methane cycling. We therefore favor oxidation of photoautotrophic-produced biomass coupled to Mn(IV)- and/or Fe(III)-reduction below the sediment-water interface as a primary carbon source for sediment pore-waters, and the early diagenetic Fe-Mn-rich carbonates with highly negative $\delta^{13}C$ values. Carbonate precipitation would have been coupled to a decrease in the initial content of TOC deposited, together with Mn(IV)- and Fe(III)-oxyhydroxides. Several models have been proposed to estimate the contribution of sediment pore-water DIC to diagenetic carbonate formation and the initial TOC content prior to MR (Heimann et al., 2010; Konhauser et al., 2017). $\delta^{13}C_{carb}$ values can help to constrain the contribution of carbon from C_{org} oxidation (DIC_{org}) and inorganic carbon from seawater (DIC_{sw}) to the total DIC_T concentration in sediment pore-waters. Samples of the Mozaan Group have $\delta^{13}C_{carb}$ values between −22.3 and −13.5 ‰ and most of them plot below the $DIC_{org} = DIC_{sw}$ line (Fig. 4). A rough estimate of contributions to sediment pore-water DIC can be obtained with the following equation (cf. Konhauser et al., 2017):

$$[DIC]_{carb}\,\delta^{13}C_{carb} = [DIC]_{org}\,\delta^{13}C_{org} + [DIC]_{sw}\,\delta^{13}C_{sw}$$

Assuming that the $\delta^{13}C$ value of Archean DIC_{SW} is near-to-zero, DIC_{org} (flux of DIC from oxidation of OM during MR) varied between 52 and 61 % DIC_T (57 % on average), while DIC_{SW} (flux of DIC from seawater) has an average of 43 % DIC_T (Table 1). In view of this,

TOC* (the initially deposited amount of TOC, which is the sum between DIC_{org} and actual TOC of the sample) decreased by 12 to 100 % during MR within the sediment (see %TOC* in Table 1).

Our carbon isotope data are similar to those for modern marginal marine environments where large amounts of OM are delivered to sediments (Berner, 1964; Konhauser et al., 2017). The example of the Santa Barbara continental margin shows that a high OM flux to sediments leads to steep vertical $\delta^{13}C_{DIC}$ gradient in pore-waters, reaching $\delta^{13}C_{DIC}$ values < −20 ‰ in the uppermost 20 cm (Berner, 1964). In contrast, areas with a lower OM flux to sediments yield higher $\delta^{13}C_{DIC}$ values ≥ −6 ‰ (Berner, 1964; Konhauser et al., 2017). The Archean marine DIC reservoir is typically considered to have been significantly larger than that of the modern oceans (e.g., Walker, 1983). If true, this would have considerably influenced sediment pore-water carbon isotope signatures, regardless of the OM flux, and should have produced early diagenetic carbonates with close-to-seawater $\delta^{13}C$ values. Such $\delta^{13}C$ values are not observed in this study. Instead, evidence for Mn-Fe-rich carbonate concretions and disseminated carbonate minerals showing overgrowths in the Mozaan Group, suggests that their formation started during early diagenesis and continued during burial diagenesis and low-grade metamorphism (Ossa Ossa et al., 2016). This formation process is consistent with oxygen isotope values of carbonate minerals, indicating further precipitation in equilibrium with sediment pore-waters at higher temperature. Our C and O isotope data indicates carbonate precipitation during diagenesis through MR below the sediment-water interface in depositional settings where OM was deposited together with Mn(IV)- and Fe(III)-oxyhydroxides that subsequently acted as electron acceptors.

5.2. Coupled stable Fe and Mo isotope systematics: evidence for aerobic Mn and Fe cycling

The isotopic fractionation of ~ +1.5 ‰ for primary Fe-oxide minerals produced by Fe(II)-oxidation in the water column through an abiotic O_2-driven pathway is similar to that imparted by anaerobic iron oxidation (e.g., photoferrotrophy; Croal et al., 2004; Johnson et al., 2008 and references therein). Dissimilatory iron reduction (DIR) below the sediment-water interface can alter δ^{56}Fe signatures of primary iron minerals and create secondary iron phases that have generally lower δ^{56}Fe values (between –0.5 and –2.5 ‰) than the initially precipitated Fe-oxide minerals (e.g., Johnson et al., 2008 and references therein). However, complete to near-complete reduction through DIR produces Fe-rich early diagenetic minerals with a similar Fe isotope composition to the precursor ferric oxyhydroxide (Johnson et al., 2008; Heimann et al., 2010; Craddock and Dauphas, 2011; Konhauser et al., 2017). Iron in shales of the White Mfolozi Inlier is mainly associated with carbonates, which lack obvious traces of ferric oxyhydroxides and therefore suggest complete to near-complete iron reduction (Fig. 2). Considering that a large fraction of re-mineralized organic carbon contributed to the pore-water DIC pool (see section 5.1.), limited exchange between dissolved pore-water Fe and the Fe reservoir of the overlying water column might be expected. In that case, δ^{56}Fe values recorded by shallow–water samples of the White Mfolozi Inlier could be inherited from the Fe mineral precursors precipitated in the water column.

Positive δ^{56}Fe values up to +1.6 ‰ of Archean IFs are commonly thought to reflect preferential removal of isotopically heavy Fe-oxyhydroxides during partial oxidation of upwelled, dissolved submarine hydrothermal Fe(II) (Rouxel et al., 2005). Experimental work has shown that precipitated Fe(III) can be 2.7 to 3.7 ‰ heavier than the residual aqueous Fe(II) pool (Icopini et al., 2004). Along redoxclines, the progressive removal of isotopically heavy Fe-oxyhydroxides leaves behind an isotopically light and depleted aqueous Fe(II) reservoir. Quantitative oxidation of Fe(II) from this depleted reservoir will lead to the precipitation of isotopically light Fe-oxyhydroxides typically associated with Mn

enrichments, as observed in some Archean and early Paleoproterozoic shallow-marine settings (Rouxel et al., 2005; Tsikos et al., 2010; Kurzweil et al 2016). Therefore, IFs deposited under redox-stratified water-column conditions are expected to show gradually decreasing δ^{56}Fe values from deep to shallow depositional settings. In the Pongola basin, a redox-stratified water column is inferred from the record of negative δ^{56}Fe values (as low as −1.27 ‰) in the more proximal setting of the White Mfolozi Inlier, indicating partial oxidation of a dissolved seawater Fe(II) reservoir. This is also the case for the tidal-flat carbonate rocks of the underlying Nsuze Group (Eickmann et al., 2018), and for associated IF of the Sinqeni Formation, deposited below the storm wave base (Planavsky et al., 2014). The latter IF even has δ^{56}Fe values within the range of late Archean sulfides (–2.0 to –1.5 ‰; Rouxel et al., 2005), suggesting that the amount of Fe precipitated as oxides represents of the order of 50 % of the aqueous Fe(II) reservoir. In contrast, higher δ^{56}Fe values between −0.48 and 0.13 ‰ are found in deeper-water shales of the Nongoma area (this study) and in felutite-ferhythmite IFs of the Nconga Formation (Smith et al., 2017).

However, the bathymetric trend in δ^{56}Fe values does not reveal the mechanism(s) for Fe(II) oxidation in the Pongola sea. Early diagenetic Mn-rich carbonates in shallow-water shales of the Mozaan Group (Figs. 2 and 3; Tables 2, S1) suggest involvement of Mn-oxyhydroxide precursors that acted as electron acceptors during MR coupled to dissimilatory manganese reduction (DMnR). Mn oxidation in natural environments occurs at a higher redox potential compared to Fe, and requires an aerobic biological catalyst for its rate to increase (Tebo et al., 2004; Learman et al., 2011). Although Mn can be oxidized with UV radiation, this process is inhibited in the presence of aqueous Fe(II), and is likely not relevant in the deposition of Mn- and Fe-rich lithologies of the Mozaan Group (cf. Anbar and Holland, 1992). Manganese oxidation through anoxygenic photosynthesis has also been proposed as a possible mechanism for pre-GOE sedimentary Mn deposits (Johnson et al.,

2013), although this model requires further testing due to the absence of modern analogues. Further questions relate to whether oxygenic or anoxygenic photosynthesis evolved first on the early Earth (Fischer et al., 2016; Cardona, 2017). However, multiple lines of evidence point towards the presence of free oxygen in the tidally influenced marine settings of the Pongola Basin (Planavsky et al., 2014; Ossa Ossa et al., 2016; Eickmann et al., 2018) as well as in the photic zone of the ~3.2 Ga Fig Tree Basin (Satkoski et al., 2015). Therefore, photosynthetically produced O_2 seems to be the most plausible agent for Mn oxidation in the Mozaan Group water column.

Another feature that supports Fe(II) and Mn(II) oxidation in shallow-marine settings relative to deeper-marine settings in the Pongola sea is the strong positive co-variation between Fe/Mn ratios and δ^{56}Fe values (Fig. 5A). Shallow-water shales of the White Mfolozi Inlier with the highest Mn concentrations are also characterized by the most negative δ^{56}Fe values, while Mn-poor shales from the deeper settings of the Nongoma area show a trend to near-zero and even positive δ^{56}Fe values (Fig. 5A). Furthermore, a positive co-variation is also observed between Fe/Mn ratios and δ^{98}Mo values, with Mn-rich, shallow-water, shales having the most negative δ^{98}Mo values (Fig. 5B). Such a positive co-variation reinforces a link between Mn precipitation and the large Mo isotope fractionation (Fig. 5B) that was previously identified for contemporaneous and younger IFs (e.g., Planavsky et al., 2014; Kurzweil et al., 2016). Mn-oxyhydroxides are known to preferentially adsorb isotopically light Mo from seawater, causing a large isotope fractionation and negative δ^{98}Mo values in manganiferous sediments associated with a Mn shuttle (e.g., Barling and Anbar, 2004). Mo adsorption on ferric oxyhydroxides might potentially represent another flux of isotopically light Mo to the sediments, but should result in a negative correlation between δ^{56}Fe and δ^{98}Mo values (e.g., Czaja et al., 2012). In this case, Fe-oxyhydroxides in deep-water settings are expected to precipitate with heavy δ^{56}Fe and lighter δ^{98}Mo values, leaving a residual

water-column with light δ^{56}Fe and heavier δ^{98}Mo values likely to be recorded in sediments deposited in shallow-water settings. Such a negative correlation is not obvious in our full dataset (Figs. 5A-C), suggesting that sorption on Fe-oxyhydroxides did not play a major role in the bathymetric trend in δ^{98}Mo values recorded in the Mozaan Group. Based on the link established here between Mn-oxyhydroxides and preferential sorption of light Mo isotopes, an absence of negative co-variation between δ^{56}Fe and δ^{98}Mo values argues against Mn(II) catalytic oxidation on ferric oxyhydroxide surfaces (cf. Lan et al., 2017).

Similar δ^{98}Mo and δ^{56}Fe values have previously been reported for the contemporaneous IF of the Sinqeni Formation deposited below wave base (Planavsky et al., 2014). This IF is also characterized by Mn enrichments, where Mn is mainly associated with manganoan siderite, while Fe is mainly hosted by manganoan siderite and disseminated coarse-grained magnetite (Ossa Ossa et al., 2016; Planavsky et al., 2014) (Fig. 2). Comparison of δ^{98}Mo and Fe/Mn values for the Sinqeni IF and other IFs as young as ca. 1.88 Ga led Planavsky et al. (2014) to interpret the observed positive co-variation as a result of preferential sorption of light Mo isotopes onto Mn-oxyhydroxides, the formation of which in the relatively shallow setting of the Pongola basin was potentially triggered by the availability of photosynthetically-produced O_2. When all Mozaan data are plotted together, negative δ^{98}Mo and δ^{56}Fe values are recorded in Mn-rich, shallow-water shales and IF (Figs. 4A and 4B). In contrast, deep-water, Fe-rich and Mn-poor shales show a trend to near-zero and positive δ^{56}Fe and δ^{98}Mo values, respectively (Figs. 4A and 4B). This pattern of isotopic signals further supports stratification in the Pongola epicontinental sea with aerobic Mn, Fe, and Mo cycles in the upper, oxidized part of the water column overlying the deep-water, anoxic (ferruginous) waters along a redoxcline (Fig. 6). Given the depositional context, the association of relatively high Mn concentrations with negative δ^{98}Mo and δ^{56}Fe values

indicates that the redoxcline was developed below the storm wave base and the site of IF deposition (Fig. 6).

5.3. Model for iron precipitation and implications for a Mn-oxyhydroxide shuttle in the water column

The combination of δ^{56}Fe, δ^{98}Mo, and δ^{13}C values and Mn concentrations suggests that shallow-water, Fe- and Mn-carbonate-rich shales and mid-depth, Mn-carbonate-rich IF of the Mozaan Group were deposited under an oxygenated water column having a pronounced Mn-redoxcline that likely fluctuated in water depth (Fig. 6). Therefore, redox conditions that controlled Fe and Mn precipitation could be described with Fe- and Mn-redoxclines (Fig. 6). The Mn-redoxcline in the upper part of the seawater column extended from the site of deposition of shallow-water Fe-Mn-carbonate-rich shales to environments characterized by deposition of Mn-carbonate-rich IF just below the storm wave base. Oxidation of significant amounts of Mn(II) requires ambient O_2, which must have been pervasive in the water column of the Pongola basin to below the storm wave base.

The strong, positive, co-variation between Mn concentrations and δ^{56}Fe values suggests a close link between Mn and Fe cycles, with progressive Fe-oxyhydroxide precipitation shifting the composition of upwelling deep-waters to higher Mn/Fe ratios and lower δ^{56}Fe values. Abiotic oxidation of Mn(II) is kinetically very slow at circumneutral pH (Learmann et al., 2011; Tebo et al., 2004). Therefore, free O_2 and Mn-oxidizing microorganisms are required to increase the rate of Mn oxidation (Learmann et al., 2011; Tebo et al., 2004). The high capacity of biogenic Mn-oxyhydroxides (e.g., poorly crystalline birnessite and vernadite) to oxidize transition metals could have contributed to Fe(II) oxidation within the Mn-redoxcline (cf. Postma, 1985). However, in the context of low

dissolved O_2 in Archean oxygen oases (cf. Olson et al., 2013) and low seawater sulfate content (Habicht et al., 2002; Crowe et al., 2014; Eickmann et al., 2018), O_2 and sulfate diffusion into sediments would have been limited. In view of this, Mn(IV)- and Fe(III)-oxyhydroxides were likely the most plausible electron acceptors for MR below the sediment-water interface during deposition of the Mozaan Group (Fig. 6). Within sediment pore-waters, Mn(II) escape to the water column would be expected under the low dissolved O_2 and sulfate concentrations. In turn, sediment pore-water Fe(II) derived from Fe(III) reduction mainly precipitated as carbonate, instead of predominantly sulfide, as in modern marine settings (Fig. 6). Seawater below the Fe-redoxcline was anoxic and ferruginous. In the Pongola basin, Fe(II) oxidation was potentially linked to direct Fe oxidation by O_2 above, and/or photoferrotrophy at, the Fe redoxcline (Fig. 6). An alternative mechanism for Fe(II) oxidation in this setting might be the reduction of shuttled Mn-oxyhydroxides below the Mn-redoxcline (cf. Dellwig et al., 2010). In this scenario, newly formed Fe-oxyhydroxides were deposited, while Mn was re-dissolved and exported to the water column.

Moreover, δ^{56}Fe values of shallow-water, Mn-rich shales and mid-depth IF of the Mozaan Group (Table 2; Figs. 3, 5, 7) are lower than values between 0.28 and 0.63 ‰ reported for the photic zone low-Fe chert of the ~3.2 Ga Manzimnyama IF, Fig Tree Group of South Africa (Satkoski et al., 2015). On the basis of a δ^{56}Fe-O_2 model (Czaja et al., 2012; Li et al., 2013; Satkoski et al., 2015), these δ^{56}Fe values of the Manzimnyama IF led Satkoski et al. (2015) to suggest that photic zone low-Fe chert was deposited under stronger oxidizing conditions (O_2 content $\leq$ 10 μM) compared to more distal deep-water high-Fe chert (O_2 content $\leq$ 0.4 μM). This δ^{56}Fe-O_2 model is less sensitive for δ^{56}Fe values lower than –0.5 ‰ (Czaja et al., 2012; Li et al., 2013; Satkoski et al., 2015) recorded in shallow-water, Mn-rich shales and mid-depth IF of the Mozaan Group. But their combined δ^{56}Fe and δ^{98}Mo values, as well as Mn concentrations may imply that average O_2 concentration of the Archean surface

ocean at ~3.0 Ga reached levels similar to or even higher than the maximum concentration of 10 μM that is usually described for Archean oxygen oases (Olson et al., 2013).

Overall, the geochemical data presented here indicate that the water column of the Pongola epicontinental sea was redox-stratified, at least during the early stage of deposition of the Mozaan Group (Fig. 6). Fe and Mo isotope trends in the Mozaan Group are similar to the ca. 2.45 Ga Koegas Subgroup of the Griqualand West Basin, South Africa (Fig. 7; Kurzweil et al., 2016). A close relationship between lighter δ^{56}Fe values and Mn precipitation has also been shown for modern Loihi Seamount deposits, precipitated from oxic seawater (Rouxel et al., 2018) (Fig.7). This lends further support to oxygenated conditions driving Mn and Fe precipitation, and thus Fe and Mo isotope fractionations, during deposition of the Mozaan Group. Maximum O_2 concentrations ≥ 10 μM were likely pervasive in the water-column up to a depth below wave base. Taken together, Mn-enrichment in ferruginous rocks of the Mozaan Group, the contemporaneous Witwatersrand Supergroup (Smith et al., 2013), and the younger, but pre-GOE, Koegas Subgroup, highlights the importance of aerobic Mn cycling during the deposition of IFs before the GOE.

6. Conclusion

Geochemical data indicate that the Pongola epicontinental sea was redox-stratified during deposition of the Mozaan Group. The well-oxygenated conditions were pervasive in the water column, spanning from the sea surface to a depth below storm wave base. Upwelled Mn(II) and Fe(II) dissolved in deep, anoxic waters were oxidized in the presence of free oxygen in the shallower part of the water column. Progressive precipitation of iron oxyhydroxides, as anoxic deep-waters upwelled through the Fe-redoxcline, resulted in Fe-depletion, high Mn/Fe ratios, and a shift to more negative δ^{56}Fe values in dissolved iron. A

Mn-redoxcline developed above the Fe-redoxcline as a significant portion of Fe was removed and dissolved oxygen content increased.

Abiotic Mn(II) oxidation by free oxygen is kinetically very slow at circumneutral pH. Therefore, Mn-oxidizing microorganisms likely played a key role in sustaining Mn cycling in the upper part of the water column, where shuttled Mn-oxyhydroxides likely contributed to further Fe(II) oxidation. However, Fe(II) oxidation by O_2 and photoferrotrophy at the Fe-redoxcline, probably aided by Mn shuttling from the Mn-redoxcline, drove deposition of Mn-poor and Fe-rich shales in deep, anoxic marine environments.

Acknowledgments:

This study was funded by the University of Johannesburg, the National Research Foundation of South Africa (DST Innovation Research Fellowship to F. Ossa Ossa; Grant 75892 to A. Hofmann and the Centre of Excellence for Integrated Mineral and Energy Resource Analysis–CIMERA Grant 91487 to the University of Johannesburg), the German Research Foundation DFG (Grant SCHO1071/7-1 to Ronny Schoenberg, University of Tübingen under the DFG-Priority Programme SPP-1833 “Building a Habitable Earth”), and the University of Lausanne. AH thanks Acclaim Exploration NL and AngloGold Ashanti for access to drill core samples. Participation by AB was supported by Discovery and Accelerator Grants from the Natural Sciences and Engineering Research Council of Canada (NSERC). We also thank the Editor for handling our manuscript and Andrew D. Czaja, for relevant and useful comments.

References

Anbar, A.D., Duan, Y., Lyons, T.W., Arnold, G.L., Kendall, B., Creaser, R.A., Kaufman, A.J., Gordon, G.W., Scott, C., Garvin, J., Buick, R., 2007. A whiff of oxygen before the Great Oxidation Event? *Science* **317**, 1903–1906.

Anbar, A.D., Holland, H.D., 1992. The photochemistry of manganese and the origin of banded iron formations. *Geochim. Cosmochim. Acta* **56**, 2595–2603.

Barling, J., Anbar, A., 2004. Molybdenum isotope fractionation during adsorption by manganese oxides. *Earth Planet. Sci. Lett.* **217**, 315–329.

Bekker, A., Planavsky, N., Krapež, B., Rasmussen, B., Hofmann, A., Slack, J.F., Rouxel, O.J., Konhauser, K.O., 2014. Iron formations: Their origins and implications for ancient seawater chemistry. In: Holland, H.D., Turekian, K.K. (Eds.), Treatise of Geochemistry, second ed. *Elsevier* **9**, 561–628.

Bekker, A., Holland, H.D., Wang, P.-L., Rumble, D., Stein, H.J., Hannah, J.L., Coetzee, L.L., Beukes, N.J., 2004. Dating the rise of the atmospheric oxygen. *Nature* **427**, 117–120.

Berner, R. A., 1964. An idealized model of dissolved sulfate distribution in recent sediments. *Geochim. Cosmochim. Acta* **28**, 1497–1503.

Beukes, N. J., Cairncross, B., 1991. A lithostratigraphic-sedimentological reference profile for the late Archaean Mozaan Group, Pongola Sequence: application to sequence stratigraphy and correlation with the Witwatersrand Supergroup. *South Afr. J. Geol.* **94**, 44–69.

Beukes, N. J., Gutzmer, J., 2008. Origin and paleoenvironmental significance of major iron formations at the Archean-Paleoproterozoic boundary. *Rev. Econ. Geol.***15**, 5–47.

Brand, W.A., Coplen, T.B., Vogl, J., Rosner, M., Prohaska, T., 2014. Assessment of international reference materials for isotope-ratio analysis (IUPAC Technical Report). *Pure Appl. Chem.* **86**, 425–467.

Cardona, T., 2017. Photosystem II is a Chimera of Reaction Centers. *J. Mol. Evol.* **84**, 149–151.

Craddock, P.R., Dauphas, N., 2011. Iron and carbon isotope evidence for microbial iron respiration throughout the Archean. *Earth Planet. Sci. Lett.* **303**, 121–132.

Croal, L.R., Johnson, C.M., Beard, B.L., Newman, D.K., 2004. Iron isotope fractionation by Fe(II)-oxidizing photoautotrophic bacteria. *Geochim. Cosmochim. Acta* **68**, 1227–1242.

Crowe, S. A., Paris, G., Katsev, S., Jones, CA., Kim, S-T., Zerkle, A. L., Nomosatryo, S., Fowle, D. A., Adkins, J. F., Sessions, A. L., Farquhar, J., Canfield, D. E., 2014. Sulfate was a trace constituent of Archean seawater. *Science* **346**, 735–739.

Czaja, A.D., Johnson, C.M., Roden, E.E., Beard, B.L., Voegelin, A.R., Nägler, T.F., Beukes, N.J., Wille, M., 2012. Evidence for free oxygen in the Neoarchean ocean based on coupled iron–molybdenum isotope fractionation. *Geochim. Cosmochim. Acta* **86**, 118–137.

Dellwig, O., Leipe, T., März, C., Glockzin, M., Pollehne, F., Schnetger, B., Yakushev, E.V., Böttcher, M.E., Brumsack, H.-J., 2010. A new particulate Mn–Fe–P-shuttle at the redoxcline of anoxic basins. *Geochim. Cosmochim. Acta* **74**, 7100–7115.

Eglington, B. M., Talma, A. S., Marais, S., Matthews, P. E., Dixon, J. G. O., 2003. Isotopic composition of Pongola Supergroup limestones from the Buffalo River gorge, South Africa: constraints on their regional depositional setting. *South Afr. J. Geol.* **106**, 1–10.

Eickmann, B., Hofmann, A., Wille, M., Bui, T. H., Wing, B. A., Schoenberg, R., 2018. Isotopic evidence for oxygenated Mesoarchaean shallow oceans. *Nat. Geosci.* **11**, 133–138.

Farquhar, J., Bao, H., Thiemens, M., 2000. Atmospheric influence of Earth's earliest sulfur cycle. *Science* **289**, 756–758.

Fischer, W. W., Hemp, J., Johnson, J. E., 2016. Evolution of oxygenic photosynthesis. *Annu. Rev. Earth Planet. Sci.* **44**, 647–683.

Goldberg,T., Gordon, G., Izon, G., Archer, C., Pearce, C. R., McManus, J., Anbar, A. D., Rehkämper, M., 2013. Resolution of inter-laboratory discrepancies in Mo isotope data: an intercalibration. *J. Anal. At. Spectrom.* **28**, 724–735.

Habicht, K.S., Gade, M., Thamdrup, B., Berg, P., Canfield, D.E., 2002. Calibration of the sulfate levels in the Archean ocean. *Science* **298**, 2372–2374.

Heimann, A., Johnson, C.M., Beard, B.L., Valley, J.W., Roden, E.E., Spicuzza, M.J., Beukes, N.J., 2010. Fe, C, and O isotope compositions of banded iron formation carbonates demonstrate a major role for dissimilatory iron reduction in ~ 2.5 Ga marine environments. *Earth Planet. Sci. Lett.* **294**, 8–18.

Hicks, N., Hofmann, A., 2012. Stratigraphy and Provenance of the auriferous-uraniferous, fluvial to shallow-Marine Sinqeni Formation, Mozaan Group, Northern KwaZulu-Natal, South Africa. *South Afr. J. Geol.***115**, 327–344.

Icopini, G. A., Anbar, A.D., Ruebush, S. S., Tien, M., Brantley, S. L., 2004. Iron isotope fractionation during microbial reduction of iron: the importance of adsorption. *Geology* **32**, 205–8.

Jiménez-López, C., Romanek, C. S., 2004. Precipitation kinetics and carbon isotope partitioning of inorganic siderite at 25°C and 1 atm. *Geochim. Cosmochim. Acta* **68,** 557–571.

Johnson, C.M., Beard, B.L., Klein, C., Beukes, N.J., Roden, E.E., 2008. Iron isotopes constrain biologic and abiologic processes in banded iron formation genesis. *Geochim. Cosmochim. Acta* **72**, 151–169.

Johnson, J.E., Webb, S.M., Thomas, K., Ono, S., Kirschvink, J.L., Fischer, W.W., 2013. Manganese-oxidizing photosynthesis before the rise of cyanobacteria. *Proc. Natl. Acad. Sci. USA* **110**, 11238–11243.

Kappler, A., Pasquero, C., Konhauser, K.O., Newman, D.K., 2005. Deposition of banded iron formations by anoxygenic phototrophic Fe(II)-oxidizing bacteria. *Geology* **33**, 865–868.

Klein C., Beukes, N.J., 1989. Geochemistry and sedimentology of a facies transition from limestone to iron-formation in the early Proterozoic Transvaal Supergroup, South Africa. *Econ. Geol.* **84**, 1733–1774.

Konhauser, K. O., Planavsky, N. J., Hardisty, D. S., Robbins, L. J., Warchola, T. J., Haugaard, R., Lalonde, S. V., Partin, C. A., Oonk, P. B. H., Tsikos, H., Lyons, T. W., Bekker, A., Johnson, C. M.., 2017. Iron formations: A global record of Neoarchaean to Palaeoproterozoic environmental history. *Earth-Sci. Rev.* **172**, 140–177.

Kurzweil, F., Wille, M., Gantert, N., Beukes, N.J., Schoenberg, R., 2016. Manganese oxide shuttling in pre-GOE oceans – evidence from molybdenum and iron isotopes. *Earth Planet. Sci. Lett*. **452**, 69–78.

Kurzweil, F., Wille, M., Schoenberg, R., Taubald, H., Van Kranendonk, M.J., 2015. Continuously increasing delta Mo-98 values in Neoarchean black shales and iron formations from the Hamersley Basin. *Geochim. Cosmochim. Acta* **164**, 523–542.

Lan, S., Wang, X., Xiang, Q., Yin, H., Tan, W., Qiu, G., Liu, F., Zhang, J., Feng, X., 2017. Mechanisms of Mn(II) catalytic oxidation on ferrihydrite surfaces and the formation of manganese (oxyhydr)oxides. *Geochim. Cosmochim. Acta* **211**, 79–96.

Learman, D. R., Wankel, S. D., Webb, S. M., Martinez, N., Madden, A. S., Hansel, C. M., 2011. Coupled biotic–abiotic Mn(II) oxidation pathway mediates the formation and structural evolution of biogenic Mn oxides. *Geochim. Cosmochim. Acta* **75**, 6048–6063.

Lyons, T.W., Reinhard, C.T., Planavsky, N.J., 2014. The rise of oxygen in Earth's early ocean and atmosphere. *Nature* **506**, 307–315.

Moeller, K., Schoenberg, R., Grenne, T., Thorseth, I.H., Drost, K., Pedersen, R.B., 2014. Comparison of iron isotope variations in modern and Ordovician siliceous Fe oxyhydroxide deposits. *Geochim. Cosmochim. Acta* **126**, 422–440.

Nägler, T.F., Anbar, A.D., Archer, C., Goldberg, T., Gordon, G.W., Greber, N.D., Siebert, C., Sohrin, Y., Vance, D., 2014. Proposal for an international molybdenum isotope measurement standard and data representation. *Geostand. Geoanal. Res*. **38**, 149–151.

Nhleko, N., 2003. The Pongola Supergroup of Swaziland. PhD thesis of Rand Afrikaans University, pp. 299.

Olson, S.L., Kump, L.R., Kasting, J.F., 2013. Quantifying the areal extent and dissolved oxygen concentrations of Archean oxygen oases. *Chem. Geol.* **362**, 35–43.

Ossa Ossa, F., Hofmann, A., Vidal, O., Kramers, J.D., Belyanin, G. Cavalazzi, B., 2016. Unusual manganese enrichment in the Mesoarchean Mozaan Group, Pongola Supergroup, South Africa. *Precambrian Res.* **281**, 414–433.

Pavlov, A. A., Kasting, J. F., 2002. Mass-independent fractionation of sulfur isotopes in Archean sediments: Strong evidence for an anoxic Archean atmosphere. *Astrobiology* **2**, 27–41.

Planavsky, N. J., Asael, D., Hofmann, A., Reinhard, C. T., Lalonde, S. V., Knudsen, A., Wang, X., Ossa Ossa, F., Pecoits, E., Smith, A. J. B., Beukes, N. J., Bekker, A., Johnson, T. M., Konhauser, K. O., Lyons, T. W., Rouxel, O., 2014. Evidence for oxygenic photo-synthesis half a billion years before the Great Oxidation Event. *Nat. Geosci.* **7**, 283–286.

Postma, D., 1985. Concentration of Mn and separation from Fe in sediments–I. Kinetics and stoichiometry of the reaction between birnessite and dissolved Fe(II) at 10 ºC. *Geochim. Cosmochim. Acta* **49**, 1023–1033.

Révész K., Landwehr, J.M., 2002. δ^{13}C and δ^{18}O isotopic composition of $CaCO_3$ measured by continuous flow isotope ratio mass spectrometry: statistical evaluation and verification by application to Devils Hole core DH- 11 calcite. *Rapid Commun. Mass Sp.* **16**, 2102–2114.

Rouxel, O.J., Bekker, A., Edwards, K.J., 2005. Iron isotope constraints on the Archean and Paleoproterozoic ocean redox state. *Science* **307**, 1088–1091.

Rouxel, O., Toner, B., Germain, Y., Glazer, B., 2018. Geochemical and iron isotopic insights into hydrothermal iron oxyhydroxide deposit formation at Loihi Seamount. *Geochim. Cosmochim Acta* **220**, 449–482.

Satkoski, A., Beukes, N.J., Li, W., Beard, B.L., Johnson, C.M., 2015. A redox-stratified ocean 3.2 billion years ago. *Earth Planet. Sci. Lett.* **430**, 43-53.

Schoenberg, R., von Blanckenburg, F., 2005. An assessment of the accuracy of stable Fe isotope ratio measurements on samples with organic and inorganic matrices by high-resolution multicollector ICP-MS. *Int. J. Mass Spectrom.* **242**, 257–272.

Shields, G., Veizer, J., 2002. Precambrian marine carbonate isotope database: Version 1.1. *Geochem. Geophy. Geosy.* **3**, doi:10.1029/2001GC000266.

Siahi, M., Hofmann, A., Master, S., Wilson, A., Mayr, C., 2018. Trace element and stable (C, O) and radiogenic (Sr) isotope geochemistry of stromatolitic carbonate rocks of the Mesoarchaean Pongola Supergroup: Implications for seawater composition. *Chem. Geol.* **476**, 389–406.

Siebert, C., Nägler, T.F., Kramers, J., 2001. Determination of molybdenum isotope fractionation by double-spike multicollector inductively coupled plasma mass spectrometry. *Geochem. Geophy. Geosy.* **2**, DOI: 10.1029/2000GC000124.

Siebert, C., Nägler, T.F., von Blanckenburg, F., Kramers, J.D., 2003. Molybdenum isotope records as a potential new proxy for paleoceanography. *Earth Planet. Sci. Lett*. **211**, 159–171.

Smith, A.J.B., Beukes, N.J., Gutzmer, J., 2013. The composition and depositional environments of Mesoarchean Iron Formations of the West Rand Group of the Witwatersrand Supergroup, South Africa. *Econ. Geol.* **108**, 111–134.

Smith, A. J. B., Beukes, N. J., Gutzmer, J., Czaja, A. D., Johnson, C. M., Nhleko, N., 2017. Oncoidal granular iron formation in the Mesoarchaean Pongola Supergroup, southern Africa: Textural and geochemical evidence for biological activity during iron deposition. *Geobiology* **15**, 731–749.

Swanner, E.D., Bayer, T., Wu, W., Hao, L., Obst, M., Sundman, A., Byrne, J.M., Michel, F.M., Kleinhanns, I.C., Kappler, A., Schoenberg, R., 2017. Iron Isotope Fractionation during Fe(II) Oxidation Mediated by the Oxygen-Producing Marine Cyanobacterium Synechococcus PCC 7002. *Environ. Sci. Technol.* **51**, 4897–4906.

Tebo B. M., Bargar J. R., Clement B. G., Dick G. J., Murray K. J., Parker D., Verity R., Webb S. M., 2004. Biogenic manganese oxides: properties and mechanisms of formation. *Annu. Rev. Earth Planet. Sci.* **32**, 287–328.

Thomson, D., Rainbird, R.H., Planavsky, N.J., Lyons, T.W., Bekker, A., 2015. Chemostratigraphy of the Shaler Supergroup, Victoria Island, NW Canada: A record of ocean composition prior to the Cryogenian glaciations. *Precambrian Res.* **263**, 232–245.

Tsikos, H., Matthews, A., Erel, Y., Moor, J.M., 2010. Iron isotopes constrain biogeochemical redox cycling of iron and manganese in a Palaeoproterozoic stratified basin. *Earth and Planetary Science Letters* **298**, 125–134.

Walker, J.C.G., 1983. Possible limits on the composition of the Archean ocean. *Nature* **302**, 518–520.

Wille, M., Kramers, J. D., Nägler, T. F., Beukes, N. J., Schröder, S., Meisel, Th., Lacassie, J. P., Voegelin, A.R., 2007. Evidence for a gradual rise of oxygen between 2.6 and 2.5 Ga from Mo isotopes and Re-PGE signatures in shales. *Geochim. Cosmochim. Acta* **71**, 2417–2435.

Wille, M., Nebel, O., Van Kranendonk, M. J., Schoenberg, R., Kleinhanns, I. C., Ellwood, M., 2013. Mo–Cr isotope evidence for a reducing Archean atmosphere in 3.46–2.76 Ga black shales from the Pilbara, Western Australia. *Chem. Geol.* **340**, 68–76.

Wilson, A. H., Zeh, A., 2018. U-Pb and Hf isotopes of detrital zircons from the Pongola Supergroup: Constraints on deposition ages, provenance and Archean evolution of the Kaapvaal Craton. *Precambrian Res.* **305**, 177–196.

Wu, W., Swanner, E.D., Kleinhanns, I.C., Schoenberg, R., Pan, Y., Kappler, A., 2017. Fe isotope fractionation during Fe(II) oxidation by the marine photoferrotroph Rhodovulum iodosum in the presence of Si – Implications for Precambrian iron formation deposition. *Geochim. Cosmochim. Acta* **211**, 307–321.

FIGURE CAPTIONS:

Fig. 1: Geological map of the Pongola basin (modified from Beukes and Cairncross, 1991) showing the locations of studied drill cores TSB07-26 and PNG2 and their

respective core logs with sample positions indicated. Drill core TSB07-26 from the White Mfolozi Inlier intersected the Sinqeni and Ntombe formations. Drill core PNG2 from the Nongoma area intersected the Sinqeni, Ntombe, and Thalu formations of the Mozaan Group.

Fig. 2: Main host minerals for reactive Fe and Mn in the Mozaan Group. (A): Back-scattered electron (BSE) image of a carbonate concretion interior from a shallow-water shale, showing Mn-rich siderite (Mn-Sd) with high Mn/Fe ratio. (B): BSE image of an interior of a thin carbonate layer from a shallow-water shale, showing Mn-Sd cement with high Mn/Fe ratio together with disseminated kutnohorite (Kut) and Fe-rich rhodochrosite (Fe-Rds). (C-D): BSE images of interiors of thin carbonate layers in IFs of the Sinqeni Formation, showing Mn-Sd with low Mn/Fe ratio together with disseminated, coarse-grained, magnetite (Mag). Magnetite grains are surrounded by Mn-Sd cement, indicating that they were present when Mn-Sd formed.

Fig. 3: Fe, Mn, and TOC concentrations combined with Fe, Mo, C, and O isotope data plotted along the lithostratigraphic columns of drill cores TSB07-26 from the White Mfolozi Inlier (shallow-water setting) and PNG2 from the Nongoma area (deeper-water setting). Shale samples from the White Mfolozi Inlier are Fe- and Mn-enriched and have the most negative δ^{56}Fe and δ^{98}Mo values. Shale samples from the Nongoma area are Fe-rich and Mn-poor and have the highest δ^{56}Fe and δ^{98}Mo values.

Fig. 4: Carbon and oxygen geochemical data for bulk carbonate (mainly Mn-siderite) in shallow-water shales from the White Mfolozi Inlier. δ^{18}O *vs* δ^{13}C plot shows values for siderite that are not in equilibrium with Archean seawater. TOC *vs* δ^{13}C plot shows measured total organic carbon (TOC) contents remaining after organic matter remineralization during diagenesis. For the two diagrams, δ^{13}C values show various organic carbon (C_{org}) and seawater inorganic carbon (C_{sw}) proportions, where most data plot close to the C_{org}:C_{sw} = 1:1 line of Heimann et al. (2010). δ^{18}O values show a trend of depletion linked to further carbonate precipitation in equilibrium with sediment pore-waters at higher temperature during late diagenesis and metamorphism.

Fig. 5: Fe, Mn, and Mo geochemical data of shales and IFs from the White Mfolozi Inlier (shallow-water setting) and the Nongoma area (deeper-water setting). (A) δ^{56}Fe *vs* Fe/Mn plot shows a strong positive co-variation. (B) δ^{98}Mo *vs* Fe/Mn plot shows a positive co-variation. (C) δ^{98}Mo *vs* δ^{56}Fe plot shows no significant co-variation. (D-F) Al_2O_3 content shows no obvious relationship with δ^{56}Fe and δ^{98}Mo values or Mo content, indicating a minimal effect of detrital input on the recorded isotope compositions or Mo content. Data of IFs are from Planavsky et al. (2014) and represent drill core samples of the Sinqeni Formation in the White Mfolozi Inlier (the same drill core as studied here). Overall, shallow-marine lithologies (shales and IFs) with higher Mn concentrations are characterized by the more negative δ^{98}Mo and δ^{56}Fe values, while deeper-water shales with low Mn content have the more positive δ^{98}Mo and δ^{56}Fe values.

Fig. 6: Seawater redox conditions and Mn-Fe-Mo cycling in marine environments during deposition of the Mozaan Group. Coupled Mo and Fe isotope systematics with Mn concentrations indicate that the shallow part of the Pongola epicontinental sea was characterized by a thick Mn-redoxcline overlying the Fe-redoxcline where Mn- and Fe-oxyhydroxides formed. Deep-waters remained anoxic to mildly oxic with high concentrations of aqueous, hydrothermally-derived Mn(II) and Fe(II), which episodically upwelled onto the shelf. Upwelling anoxic deep-waters and oxic conditions allowed progressive removal of Fe-oxyhydroxides with positive Fe isotope values leaving upwelled waters enriched in Mn and shifting Fe isotope values of aqueous Fe to more negative values. Fe(II) oxidation by dissolved, photosynthetically produced O_2, and, potentially, photoferrotrophs and shuttled Mn-oxyhydroxides at the Fe-redoxcline allowed deposition of Mn-poor and Fe-rich shales in the deep, mildly oxic to anoxic basin. The paleoenvironmental reconstruction highlights sites of deposition and associated redox conditions by combining them into a single snapshot without taking into account sea-level variations and the exact time when Mn-Fe-rich lithologies were deposited. DIR (dissimilatory iron reduction); DMnR (dissimilatory manganese reduction).

Fig. 7: Comparison of Fe, Mn, and Mo geochemical data for the Mozaan Group (Planavsky et al., 2014; this study) with those for the ca. 2.45 Ga Koegas Subgroup (Kurzweil et al., 2016) and modern oxic Loihi Seamount deposits

(Rouxel et al., 2018). (A) δ^{56}Fe *vs* Fe/Mn and (B) δ^{98}Mo *vs* Fe/Mn plots showing strong positive co-variations and suggesting redox cycling of transition metals in the presence of ambient oxygen.

Figure 1
Click here to download high resolution image

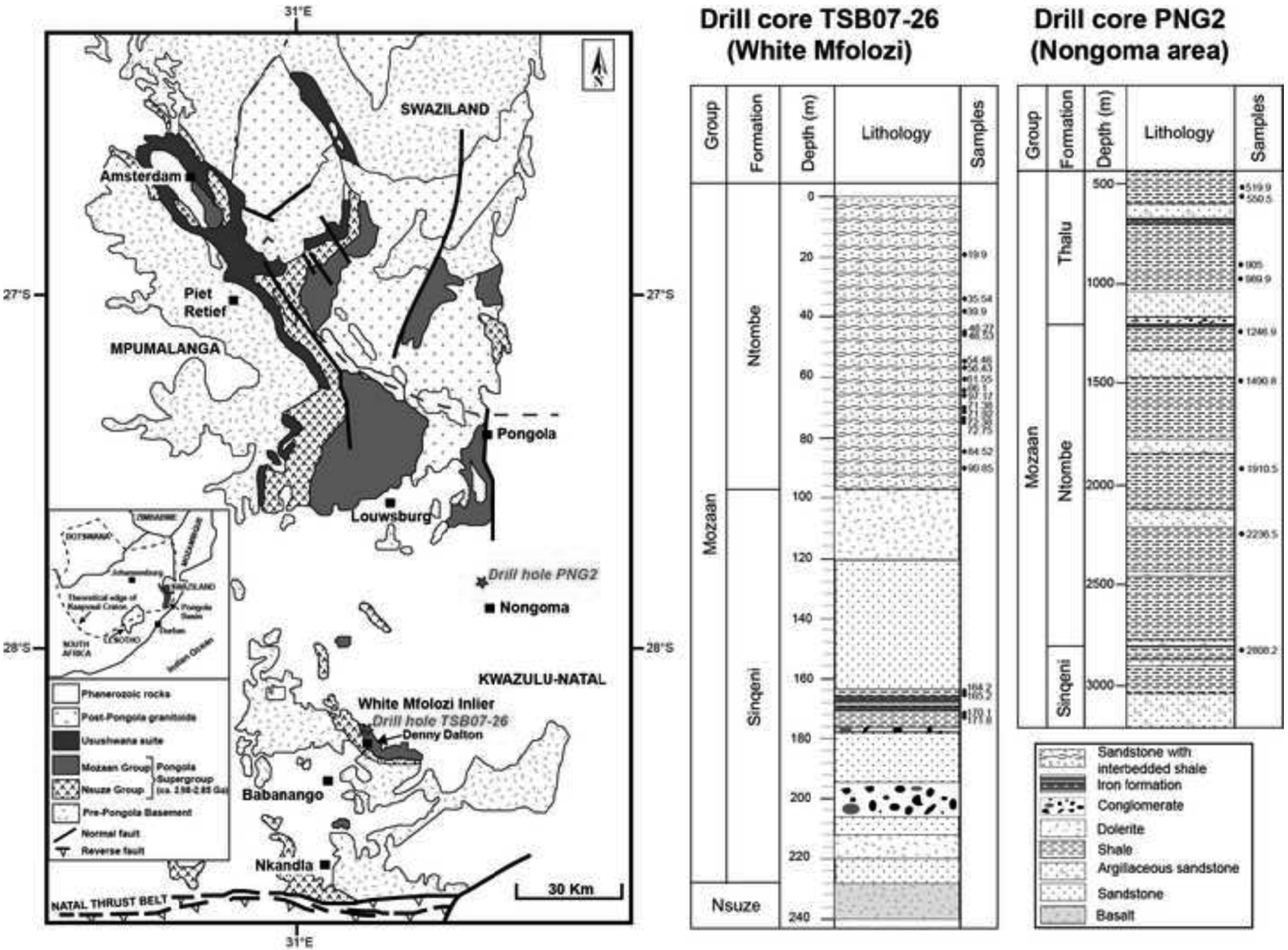

Figure 2
Click here to download high resolution image

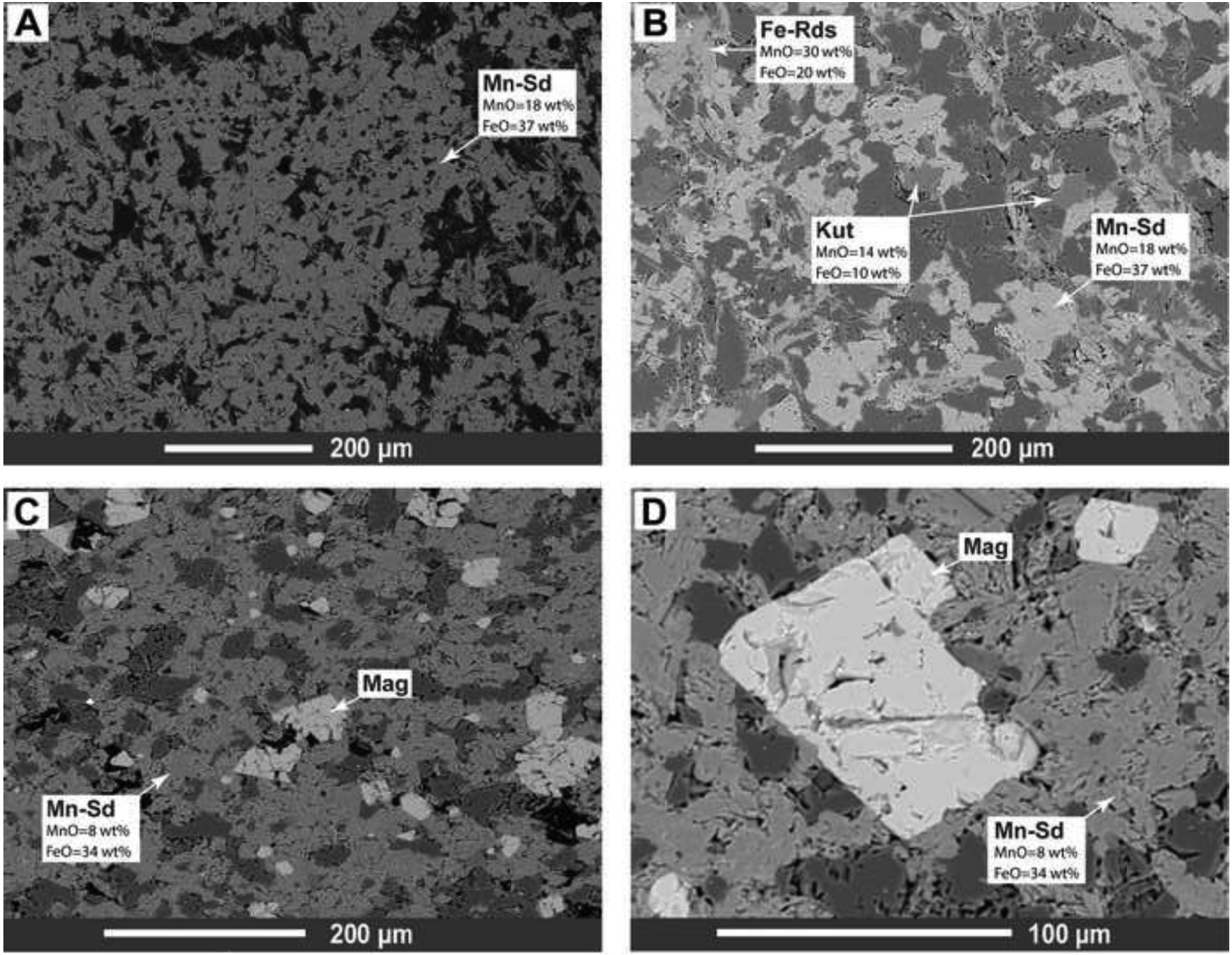

Figure 3
Click here to download high resolution image

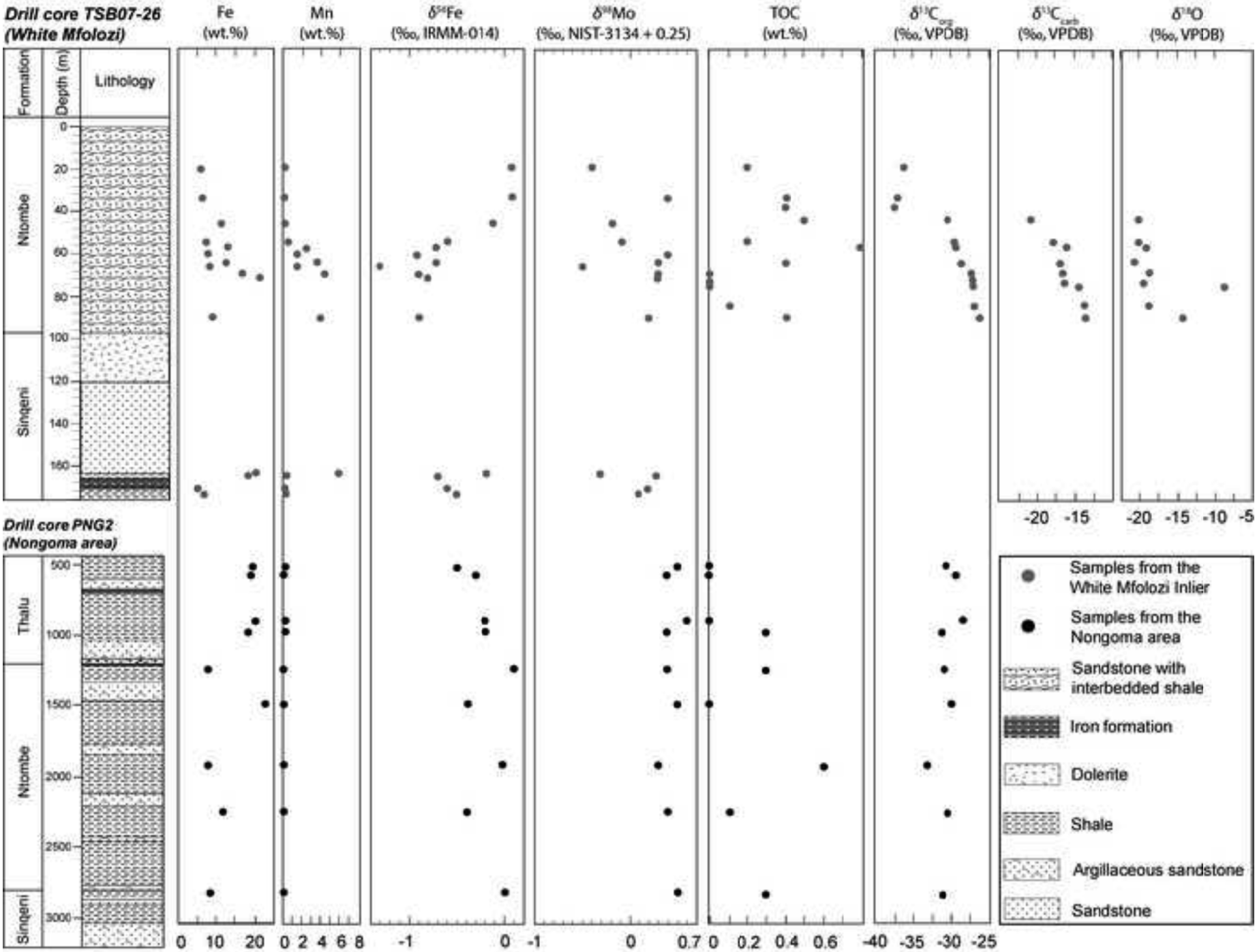

Figure 4
Click here to download high resolution image

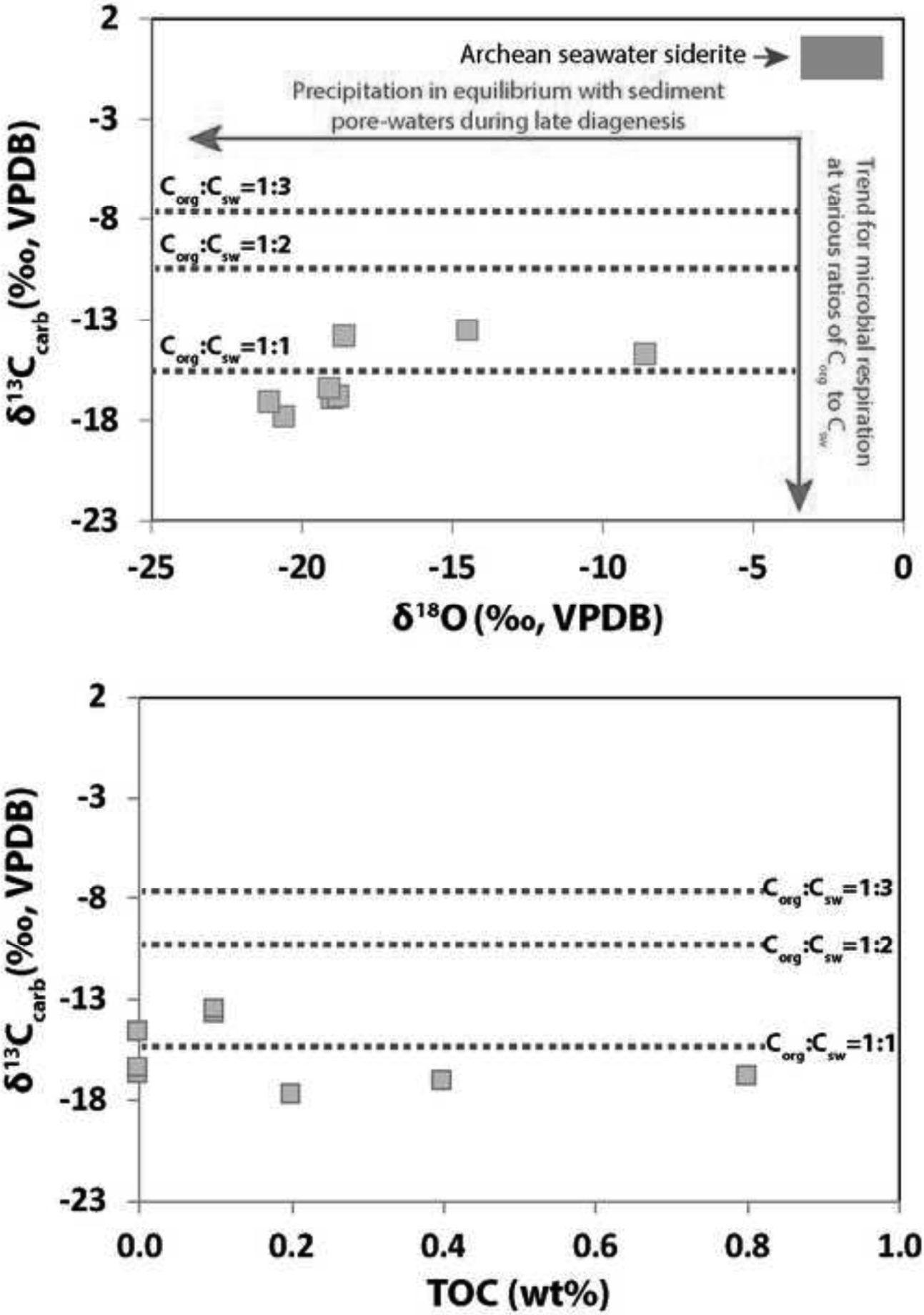

Figure 5
Click here to download high resolution image

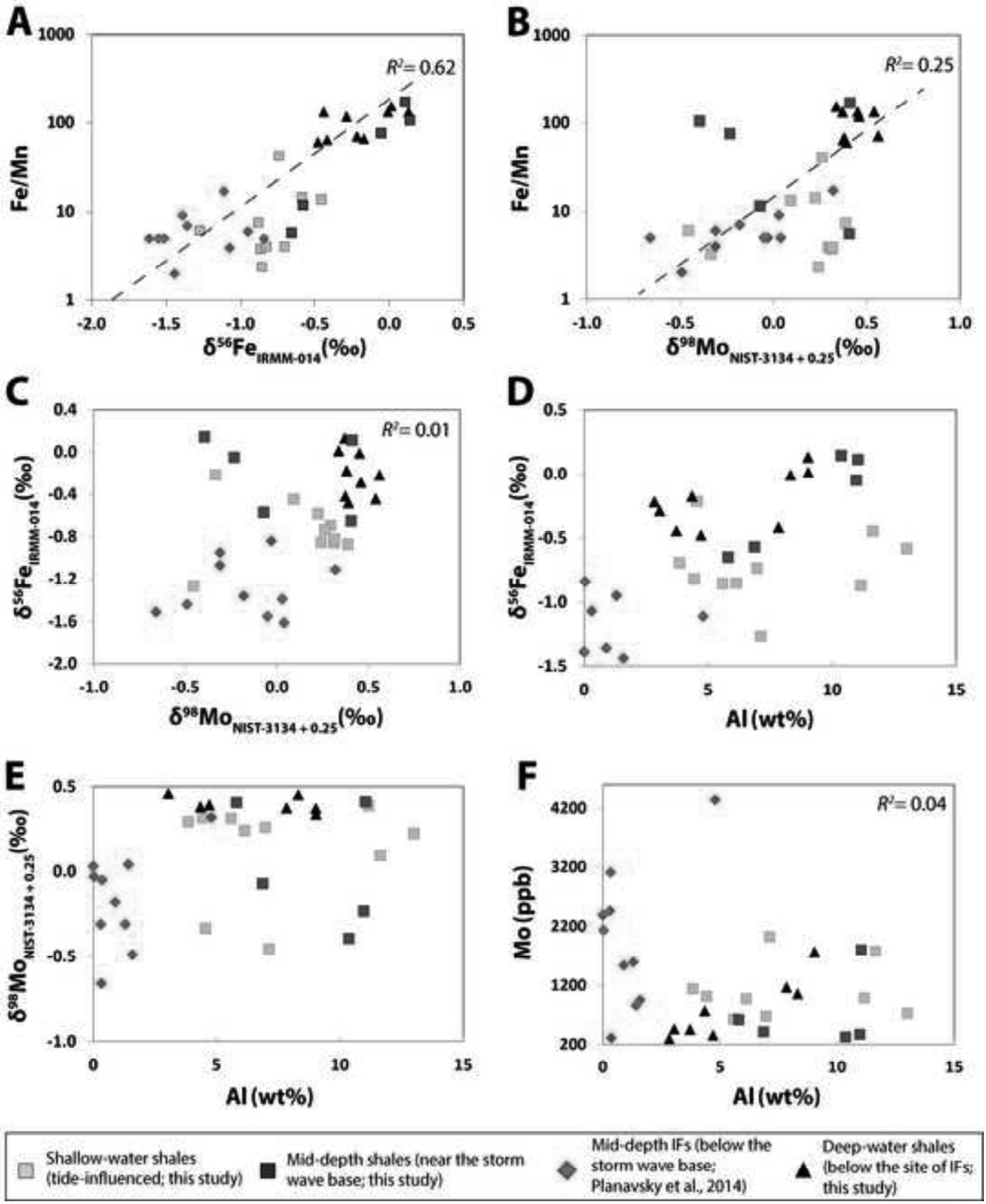

Figure 6
Click here to download high resolution image

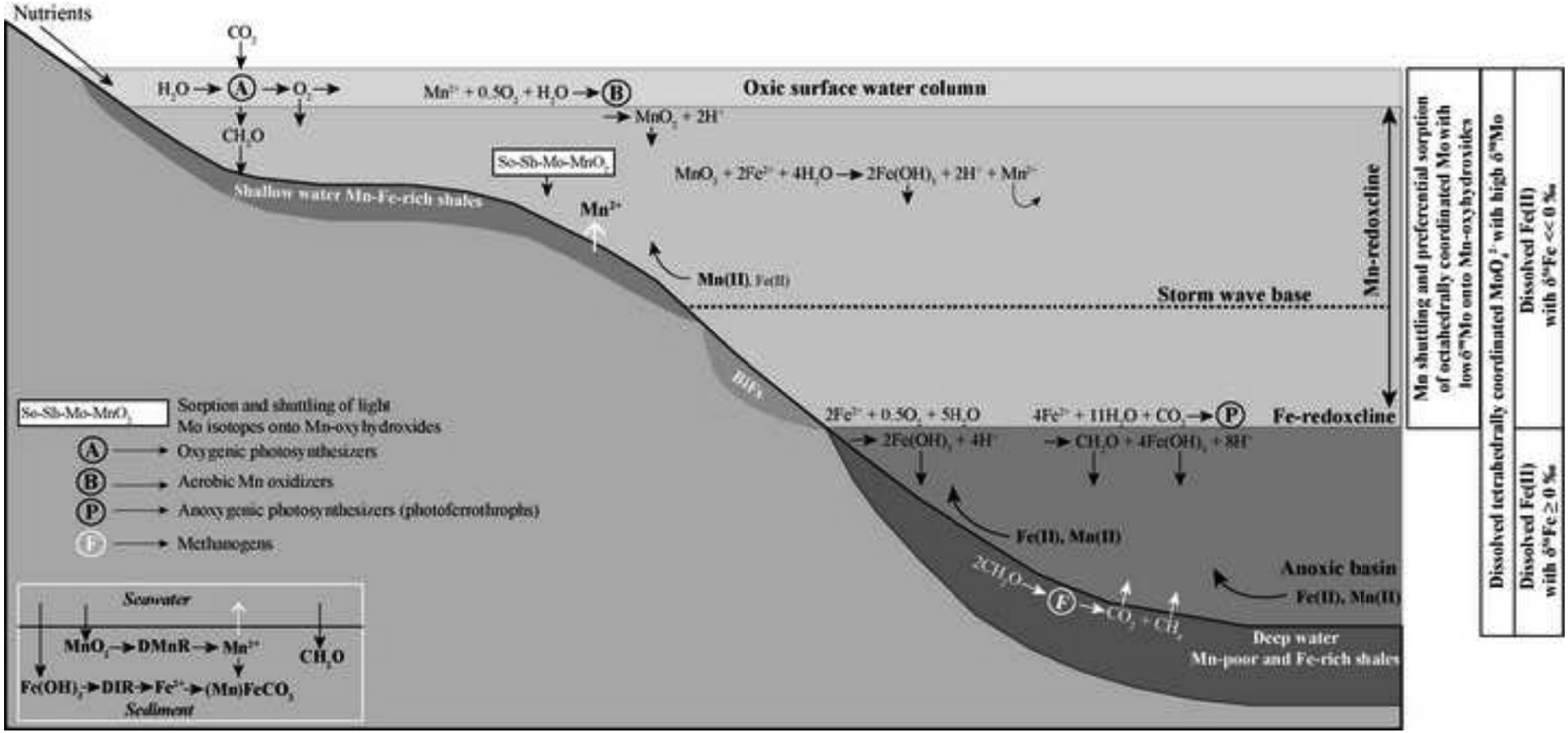

Figure 7
Click here to download high resolution image

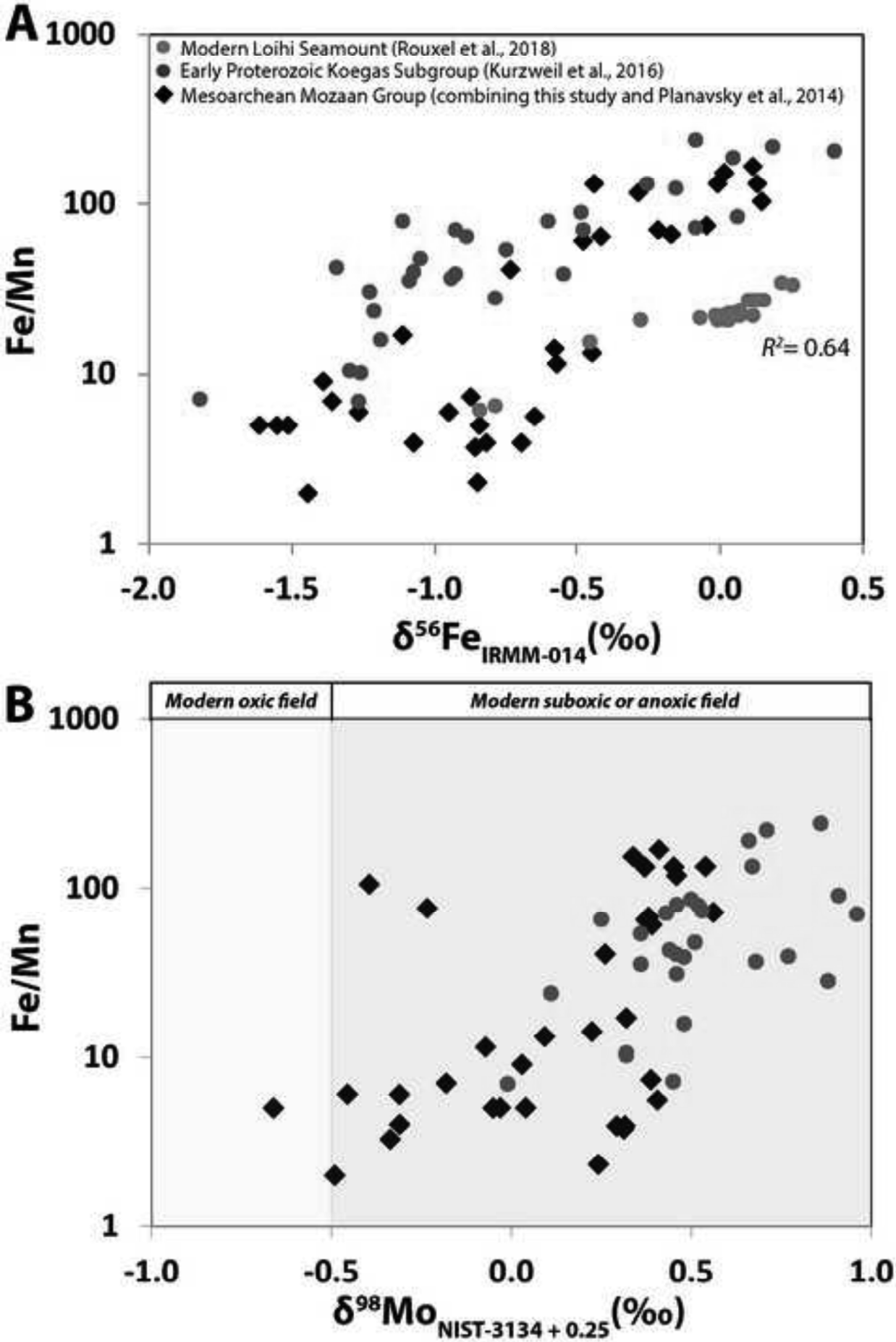

Table 1
Click here to download Table: Table 1.docx

Table 1: Carbonate and organic carbon geochemical data.

Drill core	Sample depth (m)	TIC (wt%)	TOC (wt%)	$\delta^{13}C_{org}$ (‰, VPDB)	$\delta^{13}C_{carb}$ (‰, VPDB)	$\delta^{18}O_{carb}$ (‰, VPDB)	$\delta^{18}O_{carb}$ (‰, SMOW)	$[DIC]_{org}$ (wt%)	% $[DIC]_{org}$/TIC (%)	TOC* (wt%)	%TOC* (%)
White Mfolozi Inlier (shallow-water setting)											
TSB07-26	19.9	nd	0.2	-36	-	-	-	-	-	-	-
TSB07-26	35.54	nd	0.4	-37.4	-	-	-	-	-	-	-
TSB07-26	39.9	nd	0.4	-37.7	-	-	-	-	-	-	-
TSB07-26	46.27	0	0.5	-31.7	-22.3	-20.5	9.8	-	-	-	-
TSB07-26	54.46	0.4	0.2	-29.7	-17.8	-20.6	9.7	0.2	59.9	0.4	54.5
TSB07-26	56.35	0.2	0.8	-29.3	-16.9	-19	11.3	0.1	57.7	0.9	12.6
TSB07-26	66.1	3	0.4	-28.7	-17.1	-21.1	9.1	1.8	59.6	2.2	81.7
TSB07-26	71.38	3.3	0	-27.4	-16.8	-18.8	11.5	2	61.3	2	100
TSB07-26	72.38	4.1	0	-27.3	-16.4	-19.1	11.2	2.5	60.1	2.5	100
TSB07-26	72.75	3.9	0	-27.1	-14.7	-8.6	22.1	2.1	54.2	2.1	100
TSB07-26	84.52	1.7	0.1	-26.2	-13.8	-18.6	11.7	0.9	52.7	1	90
TSB07-26	90.85	1.2	0.4	-25.7	-13.5	-14.5	16	0.6	52.5	1	61.2
Nongoma area (deep-water setting)											
PNG2	519.9	0.2	0	-31.3	-	-	-	-	-	-	-
PNG2	550.5	0.2	0	-29.9	-	-	-	-	-	-	-
PNG2	905	0.9	0	-28.4	-	-	-	-	-	-	-
PNG2	989.9	0.1	0.3	-31.7	-	-	-	-	-	-	-
PNG2	1246.9	0.3	0.3	-31.2	-	-	-	-	-	-	-
PNG2	1490.8	0.1	0	-30.6	-	-	-	-	-	-	-
PNG2	1910.5	0	0.6	-32.9	-	-	-	-	-	-	-
PNG2	2236.5	0	0.1	-30.8	-	-	-	-	-	-	-
PNG2	2808.2	0	0.3	-31.4	-	-	-	-	-	-	-

$[DIC]_{org}$ = inorganic carbon derived from remineralized organic carbon (corresponds to $[DIC]_{org}$ in the equation provided in the main text); %$[DIC]_{org}$/TIC = percentage of remineralized organic carbon in total inorganic carbon (with TIC = $[DIC]_{org}$ + $[DIC]_{sw}$); TOC* = initially deposited total organic carbon prior to microbial respiration (TOC* = TOC + $[DIC]_{org}$); %TOC* = percentage of consumed (remineralized) organic carbon during microbial respiration (%TOC* = ($[DIC]_{org}$/TOC*] x 100); nd = not detected; (-) = not measured.

Table 2
Click here to download Table: Table 2.docx

Table 2: Fe and Mo isotope data, Mo*, Fe, Mn, and Al concentrations, and loss on ignition (LOI after 12 hours at 600 ºC in air) of shale samples from the shallow-water setting of the White Mfolozi Inlier (above the storm wave base) and the deeper-water setting of the Nongoma area (below the storm wave base).

Drill Core	Formation	Sample Depth (m)	δ^{56}Fe (IRMM-014, ‰)	2 SE	δ^{98}Mo (NIST-3134, ‰)	δ^{98}Mo (NIST-3134 + 0.25, ‰)	2 SE	Mo* (ppm)	Fe (wt%)	Mn (wt%)	Fe/Mn	Al (wt%)	LOI (wt%)
						White Mfolozi Inlier (shallow-water setting)							
TSB07-26	**Ntombe**	19.90	0.144	0.022	-0.645	**-0.395**	0.010	0.3	5.7	0.1	104.9	10.4	2.6
TSB07-26	**Ntombe**	35.54	0.114	0.026	0.161	**0.411**	0.011	1.8	6.5	0.0	168.3	11.0	2.7
TSB07-26	**Ntombe**	46.53	-0.049	0.026	-0.483	**-0.233**	0.014	0.4	11.2	0.2	75.9	11.0	3.8
TSB07-26	**Ntombe**	54.46	-0.569	0.026	-0.321	**-0.071**	0.013	0.4	7.9	0.7	11.5	6.9	3.0
TSB07-26	**Ntombe**	56.43	-0.649	0.026	0.156	**0.406**	0.013	0.6	13.9	2.5	5.6	5.8	6.9
TSB07-26	**Ntombe**	61.55	-0.872	0.024	0.138	**0.388**	0.014	1.0	7.8	1.1	7.3	11.2	3.9
TSB07-26	**Ntombe**	66.10	-0.693	0.022	0.044	**0.294**	0.014	1.1	13.9	3.5	3.9	3.9	9.0
TSB07-26	**Ntombe**	67.17	-1.266	0.026	-0.705	**-0.455**	0.012	2.0	8.0	1.3	6.1	7.1	3.9
TSB07-26	**Ntombe**	71.38	-0.856	0.021	0.063	**0.313**	0.010	0.6	16.6	4.4	3.8	5.6	11.5
TSB07-26	**Ntombe**	71.92	-0.820	0.024	0.066	**0.316**	0.015	1.0	20.5	5.2	3.9	4.4	13.7
TSB07-26	**Ntombe**	90.85	-0.853	0.026	-0.008	**0.242**	0.013	1.0	9.1	3.9	2.3	6.1	2.8
TSB07-26	**Sinqeni**	164.20	-0.215	0.054	-0.585	**-0.335**	0.016	0.2	20.4	6.2	3.3	4.6	2.1
TSB07-26	**Sinqeni**	165.20	-0.736	0.024	0.011	**0.261**	0.013	0.7	18.3	0.5	40.7	7.0	4.4
TSB07-26	**Sinqeni**	170.10	-0.583	0.026	-0.025	**0.225**	0.011	0.7	5.1	0.4	14.1	13.0	2.5
TSB07-26	**Sinqeni**	171.80	-0.446	0.024	-0.157	**0.093**	0.013	1.8	7.0	0.5	13.2	11.6	2.9
						Nongoma area (deep-water setting)							
PNG2	**Thalu**	519.90	-0.286	0.023	0.210	**0.460**	0.013	0.4	19.0	0.3	60.4	3.1	4.1
PNG2	**Thalu**	550.50	-0.479	0.020	0.142	**0.392**	0.012	0.5	18.6	0.2	118.0	4.7	3.6
PNG2	**Thalu**	905.00	-0.218	0.024	0.311	**0.561**	0.012	0.3	20.0	0.3	71.5	2.8	5.5
PNG2	**Thalu**	989.90	-0.175	0.024	0.131	**0.381**	0.014	0.8	18.2	0.3	67.1	4.4	3.0
PNG2	**Ntombe**	1246.90	0.131	0.024	0.121	**0.371**	0.011	1.8	8.1	0.1	132.8	9.0	2.4
PNG2	**Ntombe**	1490.80	-0.443	0.025	0.290	**0.540**	0.012	0.5	23.1	0.2	133.0	3.7	2.0
PNG2	**Ntombe**	1910.50	0.012	0.027	0.088	**0.338**	0.014	1.8	8.2	0.1	153.4	9.0	1.0
PNG2	**Ntombe**	2236.50	-0.417	0.023	0.125	**0.375**	0.013	1.2	12.4	0.2	64.8	7.9	2.0
PNG2	**Sinqeni**	2808.20	-0.009	0.024	0.202	**0.452**	0.014	1.1	8.8	0.1	132.7	8.3	1.8

Mo* = LOI-corrected Mo concentrations; δ^{56}Fe and δ^{98}Mo values in the table are given to 3 digits, but rounded in the text to 2 digits for ease of reading.

Supplementary material for online publication only

Click here to download Supplementary material for online publication only: Table S1.docx